TUNABLE TERAHERTZ FISHNET METAMATERIAL

Cheng-Ling Chang

A dissertation

submitted in partial fulfillment of the

requirements for the degree of

Doctor of Philosophy

University of Washington

2012

Wei-Chih Wang, Chair

Chi-Hou Chan

Lih-Yuan Lin

Albert S Kobayashi

Ramulu Mamidala

Program Authorized to Offer Degree:

Mechanical Engineering

Abstract

A tunable fishnet metamaterial (TFMM) was designed and fabricated to prove its potential in controlling terahertz radiation (0.1 THz~10THz). A model to retrieve refractive index of single layer fishnet metamaterial (SLFM) was developed and applied to study the tunable frequency range of TFMM. Reference planes that define the material boundaries of SLFM and multilayer fishnet metamaterial (MLFM) were investigated to show that the material property of fishnet metamaterial is a function of layers. The issue of applying current model to MLFM was discussed.

The TFMM infiltrated with a voltage-controllable polymer dispersed liquid crystal (PDLC) was fabricated and tested by terahertz time domain spectroscopy (THz-TDS). An encapsulating technique that covers PDLC with a polyimide layer (skin layer) was applied to prevent volatile liquid crystal from escaping the PDLC and enable the deposition of metal layer. Concept of tuning TFMM infiltrated with PDLC (PDLC-TFMM) was proven by measuring the frequency shift in the reflection coefficient. The negative refractive index of PDLC-TFMM was achieved. The reliability issue of current PDLC-TFMM was discussed.

Acknowledgements

I want to give my deepest thanks to my supervisor Prof. Wei-Chih Wang who inspired me with this novel research project. He always encourages me to explore the unknown and challenging ideas. Without his encouragement, I wouldn't conduct such challenging research project.

I would also like to thanks Prof. Chi-Hou Chan, Prof. Edwin Pun and Prof. Jensen Li at City U. of Hong Kong who gave me the biggest support of funding, material and equipment. Without their support and advice, I wouldn't complete so many challenging tasks by myself. I would also give my thanks to Prof. Johnny C. Ho at City U. of Hong Kong and Thomas at Chinese U. Hong Kong for their support on gold material and physical deposition machine which is very expensive at this time. I want to give my special thanks to my lab mate, Fong-Ru Hsieh for his continuous support on theoretical part of my thesis. Also I would like to thank Hong-Ren Lin for his support on fabrication and willing to continue research on tunable metamaterial. Thanks to Ken Lew and Dr. Xiao Gan on helping me setup the THz-TDS in City U. of Hong Kong. I would also like to thank Polis Wong, Robust Lai, Kwok-On Tsang and Wai-Tong Chan at Optoelectronics Lab at City U. of Hong Kong for their help on not just clean room facilities and material supply but also their years of experiences on micro fabrication. Without their experiences, I will encounter more problems than I thought in fabrication. Thanks to Alvin Tsai, Xiao Lin and Fei Xiu at City U. of Hong Kong for spending time with me on E-beam machine. Thanks to Ben Estroff for his advice and help with the writing. I want to give my special thanks to Chloe W. Y. Ko for being such a good coordinator during my visit in Hong Kong.

Finally, I would like to dedicate this thesis to my parents. They are my biggest physical and mental support through my Ph.D. study.

Table of Contents

List of Figures

List of Tables

Chapter 1

Introduction to terahertz radiation and image

1.1. Introduction

Terahertz (THz) radiation is in an unique frequency range (0.1~10THz) where it can penetrate most dielectric materials without substantial attenuation [1]. THz radiation is between the infrared and microwave frequencies (Figure 1), where low-cost light sources and detectors are still under development. Thus, this frequency range is called the "THz gap". The penetrating ability of THz radiation can be utilized to observe internal material properties and construct THz image. Compared to x-rays, THz radiation is a better source for biological imaging, health monitoring, medical diagnostics and security due to its low energy level (meV versus keV, respectively) [2-12]. Another application of THz image technology is imaging and spectroscopy through materials, utilizing an established library of THz spectral signatures, called "fingerprints", to identify frequency-dependent properties that are present inside a material [13], such as different chemicals in drugs [8] or tumors in skin tissue [14].

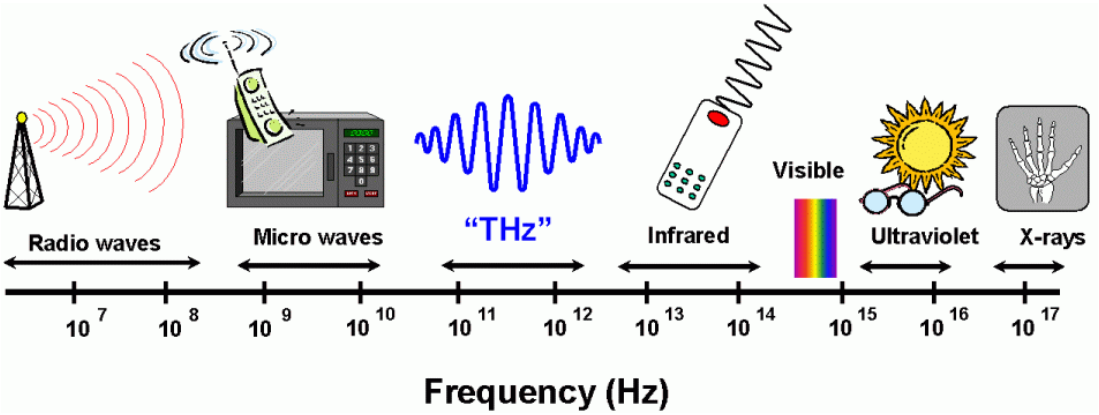

Figure 1: Electromagnetic wave spectrum

Commercial THz imaging systems, such as T-ray 4000 from Picometrix Inc. (Figure 2) is composed of a THz laser, lens system, camera and mechanical stage. It can be used to detect hidden objects, such as weapons, or find the defects in materials. Another commonly used THz imaging technique is called terahertz time domain spectroscopy (THz-TDS), shown in Figure 3. Unlike commercial THz imaging systems, the image from THz-TDS is constructed from time domain electric pulses, which excite all frequency responses in a material. THz-TDS can characterize material properties via a broadband spectral response with amplitude and phase information.

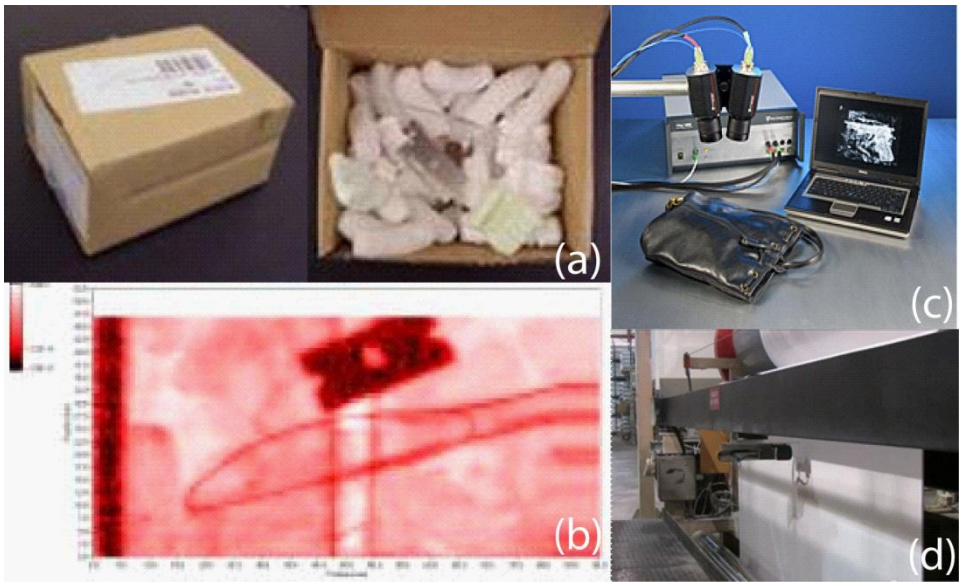

Figure 2: THz image system (a-b) shows that THz image from T-ray 4000 (Picometrix Inc.) can see a plastic knife and metal razor through packaging. (c)T-ray 4000 is composed of pigtailed fiber optic THz generator and camera that can generate THz range beams and visualize the image in real time. (d) For large area scanning like roofing plant, T-ray 4000 requires mechanical arm and shorter working distance to obtain required resolution and power.

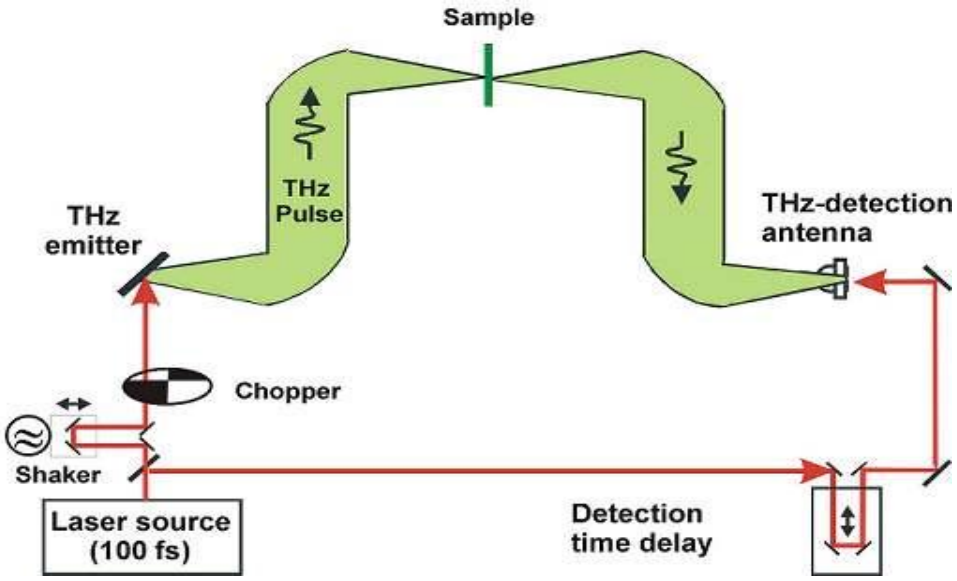

Figure 3: THz-TDS system provides amplitude and phase over a broadband spectral range.

1.2. Background

With rapid growth of applying THz image technology to various fields, there is a major shortcoming of current commercial THz imaging systems: cumbersome mechanical stages. The mechanical stages move either the light source or the sample to complete a two-dimensional image scanning. The scanning speed and accuracy of commercial THz imaging systems [6, 15] can be greatly enhanced and made less costly if the mechanical stage is replaced by an THz beam steering device.

An example of a beam steering device based on electro-optic (EO) polymer [16, 17] is shown in Figure 4. Here, an EO prism utilizes a refractive index change to deflect the beam in a different direction when an external electric field is applied. The scanning frequency is determined by how fast the EO polymer can respond, which is usually in MHz [18]. Also, the beam steering angle is determined by the refractive index change (Δn) of the EO polymer. However, the refractive index of the EO polymer [16] is usually far less than 0.01, resulting a small deflecting angle. Consequently, a material that can generate large Δn is the key to ultra wide beam steering devices.

Metamaterial seems to be a good candidate to generate large Δn because the refractive index of metamaterial is highly sensitive to parameters such as incident

wavelength or geometry. For example, the refractive index of fishnet metamaterial can be changed from 0.7 to -1.5 when the incident wavelength varies from 1200nm to 1760nm [19]. Also, when the incident wave is operated at 0.8THz and the dimension of fishnet pattern is modified, the ideal Δn can reach as high as 5 [20].

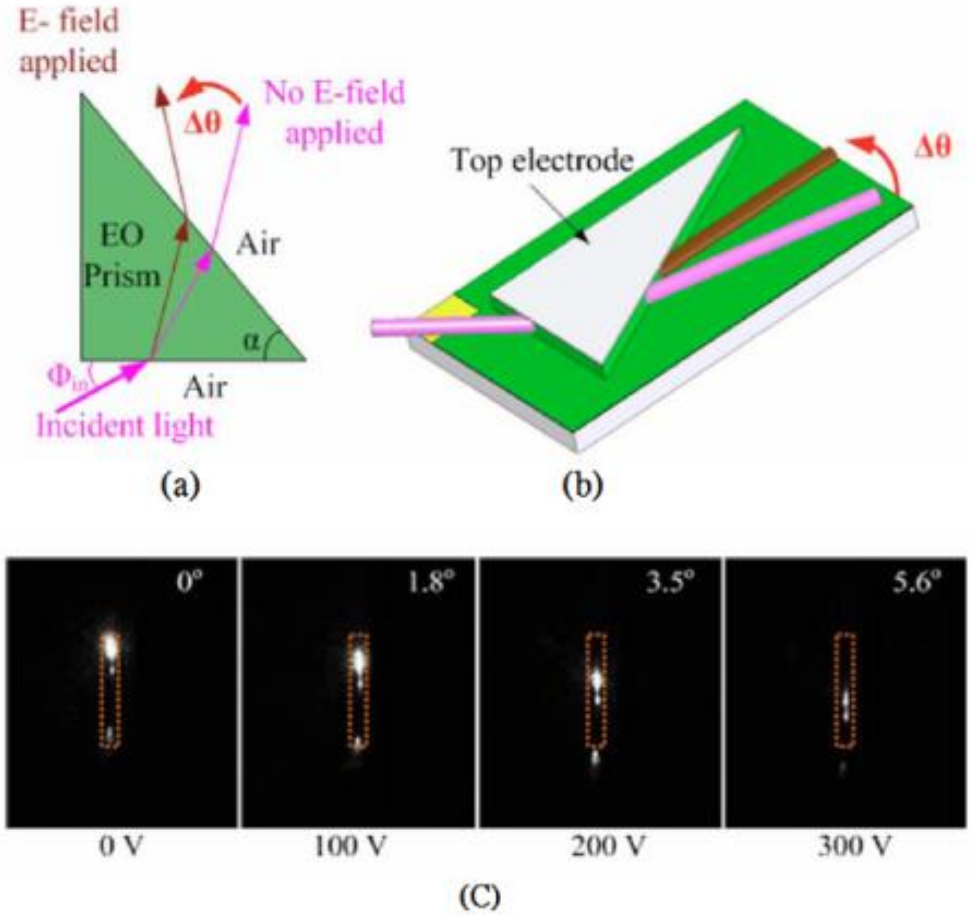

Figure 4: (a-b) Design of electro-optical polymer based prism deflector (c) The experimental results of deflected angle versus applied voltage.

1.3. Motivation

This study was motivated by a desire to design, fabricate and test a novel tunable fishnet metamaterial (TFMM) which can be potentially applied to beam steering and eventually improve current terahertz image systems [21]. TFMM with large tunable

refractive indices can be the foundation of not just terahertz image systems, but also terahertz communication systems, such as THz modulators.

The uniqueness of the designed TFMM is the use of polymer dispersed liquid crystals (PDLC) [20] and a process developed to seal the liquid crystals in the PDLC so that device does not require a confined liquid crystal cell. With a large dielectric constant change in the PDLC, TFMM can achieve a large Δn. The soft and flexible nature of PDLC and the polymer skin layer enable the device to be made to conform to a non-planar surface, an important advantage for compact (and possibly wearable) sensing applications. Furthermore, TFMM is scalable, meaning that there is no limit on operating frequency. Hence, the concepts behind using TFMM infiltrated with PDLC in the THz range can also apply to the optical range.

1.4. Summary

The work is primarily focused in two efforts: the first aims at a comprehensive understanding of the modeling of fishnet metamaterial and the second focuses on developing a TFMM infiltrated with PDLC. Chapter 1 introduces background, motivation, objective and proposed approaches. Chapter 2 describes the working principle of a typical split ring resonator (SRR) and how SRR evolves into fishnet metamaterial.

In Chapter 3, a detailed description of the liquid crystal based TFMM model with theoretical derivation of the constitutive parameters and boundary conditions will be discussed. The first section shows how to retrieve effective refractive indices from transmission and reflection coefficients. This is followed by defining the appropriate reference planes (material boundaries) by using impedance matching criterion. The next section is dedicated to an approach that can uniquely define the real part of refractive index. The tuning range of TFMM infiltrated with liquid crystal and applying the developed model to multilayer fishnet metamaterial are discussed in the last two sections.

Chapter 4 includes design, fabrication, characterizing of the fishnet metamaterial infiltrated with SU8 and PDLC. The chapter starts with the introduction of THz-TDS systems and techniques that are commonly used to retrieve refractive indices. The next section shows techniques to remove the substrate effect. The fabricated SU8 and PDLC

TFMM are shown in the last two sections. The experiment results are then compared with simulations.

Chapter 2

Tunable metamaterial

2.1. Introduction to metamaterial

The theory of negative refractive index materials(NIMs) known as metamaterials was first proposed by V.G.Veselago [22] in 1968. However, the study of metamaterials stalled due to the lack of the ability to create a material possessing simultaneous negative permittivity and permeability. In 1999, first split ring resonator (SRR) was theoretically proved to have negative permeability [23]. The first metamaterial possessing both negative permeability and permittivity was later proposed by D.R. Smith [24] in 2000. The realization of the first metamaterial prototype motivated the rapid development of new experiments and theories of metamaterials. Metamaterials have gained attention due to their ability to produce exotic electromagnetic phenomena such as negative indices of refraction, negative permittivity, and negative permeability.

Metamaterial is scalable. It can be applied to a wide frequency range from microwave to optical by tuning the geometry of the conducting periodic structure or the substrate permittivity and permeability. It can potentially be used for high gain and directional microwave devices, super lenses, imaging, bolometric wave detection [25], novel antennas, 'invisibility cloaks' [26], and surface plasmon sensors for biological and material sensing [27]. In our research, we will focus on tunable fishnet metamaterial (TFMM) as a potential element of THz beam steering. Since fishnet metamaterial is basically a modified SRR structure, we first introduce the SRR metamaterial.

SRR metamaterial is basically a frequency-sensitive electromagnetic resonator which resonates at a certain narrow frequency range. The typical SRR design is shown in Figure 5. It consists of two concentric split rings with gaps on opposite sides. If a magnetic field is introduced orthogonally to the SRR surface, it induces an electric current that flows around the split ring. In response, a magnetic resonance is induced and negative permeability is created. When another thin wire is placed behind the SRR structure, both negative permeability and permittivity are excited. In this case, the effective refractive index of the SRR and thin wire composite becomes negative [28]

The resonating phenomenon of SRR can be explained by inductance and capacitance (L&C). When the harmonically varying magnetic field passes through a metal ring, the ring generates a current that creates magnetic flux opposing the applied magnetic field [29] as shown in Figure 5a. Based on the constitutive relation (eq.1), the magnetic flux, $\tilde{B}$ in terms of magnetic field strength $\tilde{H}$ is:

$$\tilde{B} = (1 + x_{eff})\, \mu_0\, \tilde{H} \quad \ldots\ldots.(1)$$

where $\tilde{B}$ is the magnetic flux, $\mu_{eff} = 1 + x_{eff}$ is the effective permeability, μ_0 is the permeability in vacuum, x_{eff} is the susceptibility and $\tilde{H}$ is the harmonic magnetic field. To create a strong negative permeability, the metal ring structure requires a modified ring design because x_{eff} of regular ring is between zero and negative one resulting in positive μ_{eff} . When the single ring structure is cut with a gap, the gap forms a capacitor as shown in Figure 5b. This structure is equivalent to an RLC circuit and its resonant frequency can be expressed as

$$\omega_0 = \frac{2}{\sqrt{\pi r_0 L C_{pu}}} \ldots\ldots.(2)$$

where C_{pu} is the inter-ring capacitance per unit length, L the average inductance of the two rings and r_0 the average radius of the SRR. With double ring structure, the capacitance between inner ring and outer ring can further enhance the resonance. When the operational frequency goes beyond the resonant frequency, x_{eff} becomes less than -1. Hence, a negative μ_{eff} is generated (Figure 5d).

On the other hand, the permittivity of the noble metal such as gold or silver is already negative below its plasma frequency (< optical region). Thus, as long as the operating frequency is below plasma frequency, negative permittivity can be achieved. Planar electric metamaterial is a good example of this, showing that electric resonance can be induced by having a planar double ring structure facing orthogonally to the incident wave [30, 31] (Figure 6).

In typical SRR metamaterials, there will be a long metallic wire on the back side of the SRR, parallel to the incident electric field. With the presence of metallic wire and SRR, negative permittivity and permeability occur simultaneously, causing the effective refractive index to be negative. Thus, SRR was the first 'true' metamaterial. All other metamaterials such as fishnet and staple-like metamaterials [20, 32] are based on the concept of SRR metamaterial.

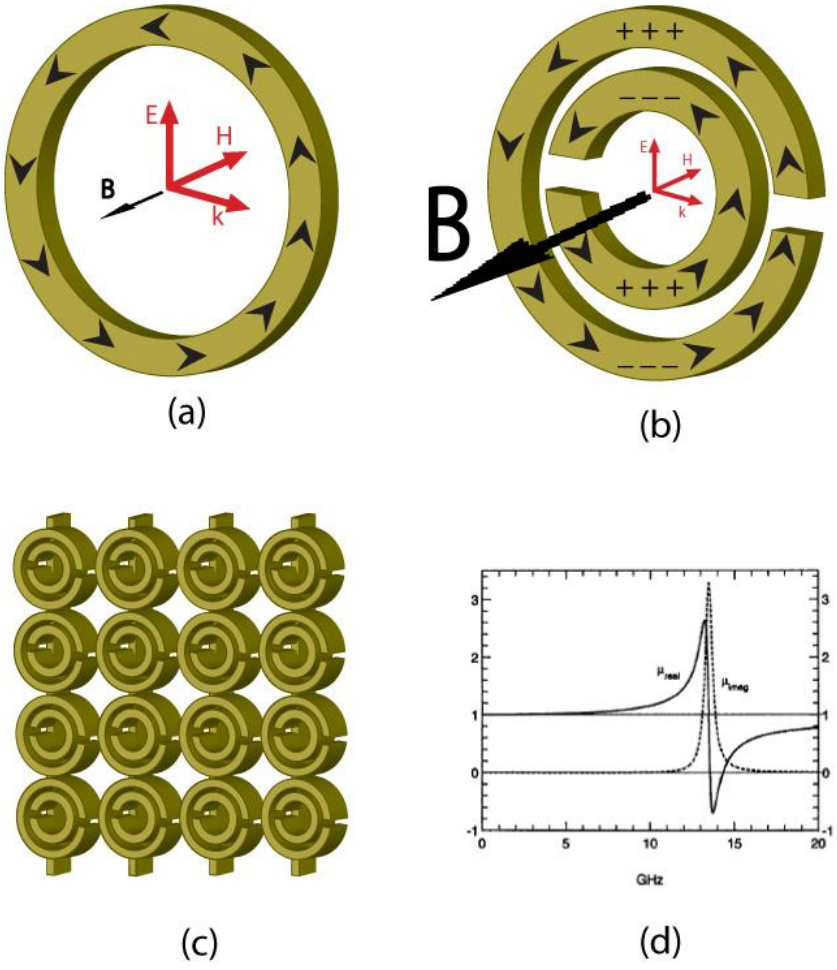

Figure 5: Split ring resonator (SRR) metamaterial: (a) the changing magnetic flux in a uncut single ring structure induces a current that generates field opposing the change in applied magnetic flux (b) SRR is a double-ring structure with cuts that form capacitors. When the SRR couples the magnetic field, it induces stronger magnetic resonance than single ring. The magnetic resonance frequency induced by

SRR is similar to an LC circuit which can be expressed in eq.2. (c) when arrays of SRR and electric wires are combined, negative permeability and permittivity occur simultaneously (d) permeability plot versus operation frequency of SRR[23] showing that real part of permeability of SRR is negative near the resonant frequency region while imaginary part of permeability is positive because the material is lossy.

2.2. From split ring resonator (SRR) to tunable planar electric metamaterial

Typical split ring resonators (SRRs) operate at a scale much smaller than the incident wavelength and can be excited by the magnetic response to achieve negative permeability. The propagation direction of the incidence wave must be parallel to the surface to obtain the maximum resonant effect. However, to fabricate multilayer structures with split ring pattern with a nicely cut plane for incidence light in optical range to enter the metamaterial is challenging at nano- and micro- meter ranges. However, this difficulty can be eliminated by utilizing a design where the wave propagates normal to the planar metamaterial surface.

One solution is using a metamaterial design that uses a symmetrical structure with two split rings facing each other (Figure 6). With the split rings arranged to symmetrically face each other, the induced out-of-plane magnetic response is cancelled and the resonating effect is an in-plane electrical response for incident normal transverse electromagnetic waves-an electric resonator [30, 33]. The resonating phenomenon is the same as SRR, as described in section 2.1. The only difference is the resonance is due the incident electrical field that is coupled by planar metamaterial. When the electrical field is perpendicular to the gap, as shown in Figure 6a, the electric field will induce a resonance which can be represented by a double RLC circuit (Figure 6b). The planar electric metamaterial only induces a negative effective permittivity. The out-of-plane magnetic field is cancelled by the symmetric double ring structure.

The planar metamaterial can also be made active. Tuning planar metamaterials by Schottky diode has been shown as an effective technique to control metamaterial responses [33]. The active planar metamaterial is fabricated (in this case, gold electric resonator elements) on a semiconductor substrate to form a Schottky diode. Upon a

voltage bias, the conductivity of the substrate at the split gaps changes from a short to an open circuit, actively controlling the charge accumulation near the gap. The active planar metamaterial by Schottky diode method can be used as a switch or modulator that controls the transmission of the incident wave. However, the change of the dielectric constant in the active planar metamaterial by this method is insufficient to achieve resonant frequency tuning. Since the planar metamaterial is equivalent to a RLC circuit, the capacitance of the gap can be varied if the semiconductor substrate is replaced by an active, variable refractive index material, such as liquid crystal or PDLC,. Thus, broadband tuning becomes possible. Based on this tunable metamaterial idea, we were interested in looking for a design with following features: (i) incident wave propagation normal to metamaterial surface and (ii) resonant frequencies tunable by the changing of the dielectric constant of the substrate material, resulting in a change of the system capacitance. The fishnet metamaterial, described in the following section, meets these criteria.

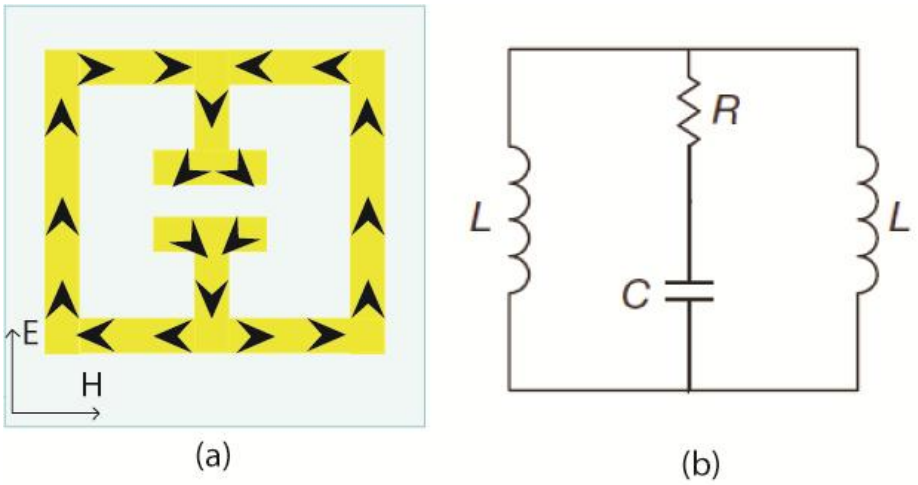

Figure 6: Planar electric metamaterial: (a) the incident wave is normal to the surface of the plane. When the electric field is perpendicular to the gap, the structure couples the electric field and creates electric resonance. The induced current (shown by the black arrows) by the electric field in the two facing rings creates an out-of-plane opposing magnetic field (b) the equivalent RLC circuit of planar electric metamaterial.

2.3. Tunable fishnet metamaterial (TFMM)

Unlike electrical metamaterial with symmetrical split rings that only allow control over permittivity, fishnet metamaterial can achieve simultaneously negative permittivity and permeability with incident planar-normal electromagnetic waves. The fishnet structure is a combination of elements with magnetic response and electric response [34] (Figure 7). The magnetic response comes from the simplified staple-like magnetic resonant structure that couples the magnetic field and generates surface current. On the other hand, the electrical response comes from the array of thin wires. If the incident electrical field is parallel to the wires, the electrical field induces a current along them and generates the electric dipoles. The electrical response from wire structure exhibits plasmonic–type electric resonance which give negative permittivity near the resonant frequency [35]. The form of magnetic resonant frequency of fishnet metamaterial can be described by eq. 3 [36].

$$f_m = \frac{\omega_m}{2\,\pi} \sim \sqrt{\frac{1}{{L_m}^2} + \frac{1}{L_m L_e}\frac{W_e}{W_m}} \ldots\ldots(3)$$

where f_m is the magnetic resonant frequency and ω_m is the angular frequency. L_m, L_e, W_m and W_e are the dimensions fishnet metamaterial shown in Figure 7d. From eq. 3, one can know that the magnetic resonant frequency increases when the width of magnetic element W_m is reduced, and eq. 3 can be used to adjust the resonant frequency of fishnet metamaterial. Simulation in the literature [20, 37] shows that the fishnet structure can be further modified into an isotropic-like structure which makes fishnet metamaterial independent to the incident wave polarization.

To make the fishnet metamaterial tunable, a similar tuning approach based on the tuning concept of planar electrical metamaterials[33] can be applied: tune the dielectric constant between the top and bottom fishnet electrodes to change the capacitance. The advantage of making fishnet metamaterial a tunable device is that the electrodes, used to apply the electric field, comes from the fishnet metamaterial itself. In the next Chapter, a

design of tunable fishnet metamaterial based on tuning the dielectric constant of liquid crystal by fishnet electrodes will be introduced.

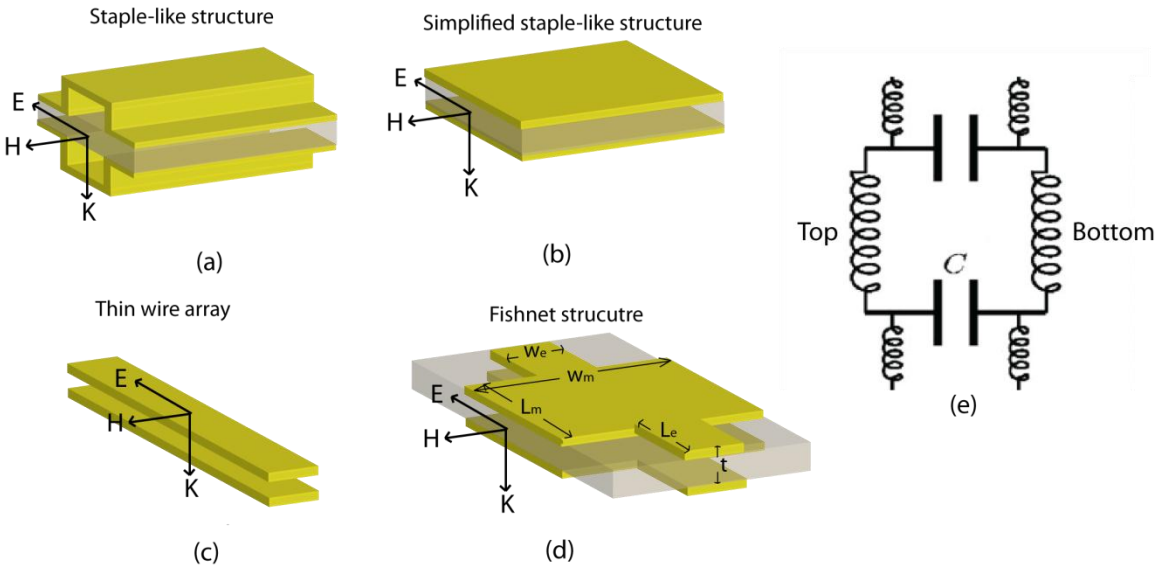

Figure 7: Fishnet structure combines the SRR-like or staple-like structure as magnetic resonant element and thin wire array as electric resonant element. Both elements have its resonant frequency (magnetic resonant frequency and electrical resonant frequency): (a) staple-like structure resemble the symmetrical 3 dimensional split ring which couple the magnetic field of the incident electromagnetic wave (b) the simplified staple-like structure flattens the staple-like structure to parallel strips which can reduce the difficulty of fabrication, especially in nanometer ranges (c) thin wire array is used to couple the electrical filed to produce negative permittivity (d) the combination of (b) and (c) gives the fishnet structure which can produce negative permeability and permittivity at the same time (e) the LC circuit model of fishnet structure.

Chapter 3
Design of tunable fishnet metamaterial (TFMM) in THz region

3.1. Single layer fishnet metamaterial (SLFM) design and simulation model

To quantify the tunability of the designed isotropic TFMM, it is necessary to create a model to calculate its refractive index. The method of retrieving the refractive index from the transmission and reflection coefficients is well-established for split ring resonators (SRR) [38] and applies to fishnet metamaterials [19, 20, 39]. In our research, the retrieving algorithm adopted a method proposed by Chen [38].

The proposed liquid crystal based tunable THz fishnet metamaterial is shown in Figure 8. Liquid crystal is used here mainly for developing the algorithm and its properties are well-studied in THz range [40]. In this design, the shape of fishnet metamaterial is pseudo-isotropic, which is not affected by the polarization of the incident wave [20].

As shown in Figure 8b, the unit cell is a square with a dimension of Ld = 150 μm. Liquid crystal is sealed between the two gold electrodes with dimension D = 106 μm. Polyimide is used in two places in the design. First, it was used as the liquid crystal cell sidewalls because the material can be easily patterned using conventional lithography. Second, the material was used as a supporting substrate for the fishnet electrodes due to its good thermal stability and mechanical strength. The thickness of the PI substrate is 4 μm, gold is 0.4 μm and the liquid crystal is 9 μm (Figure 8c).

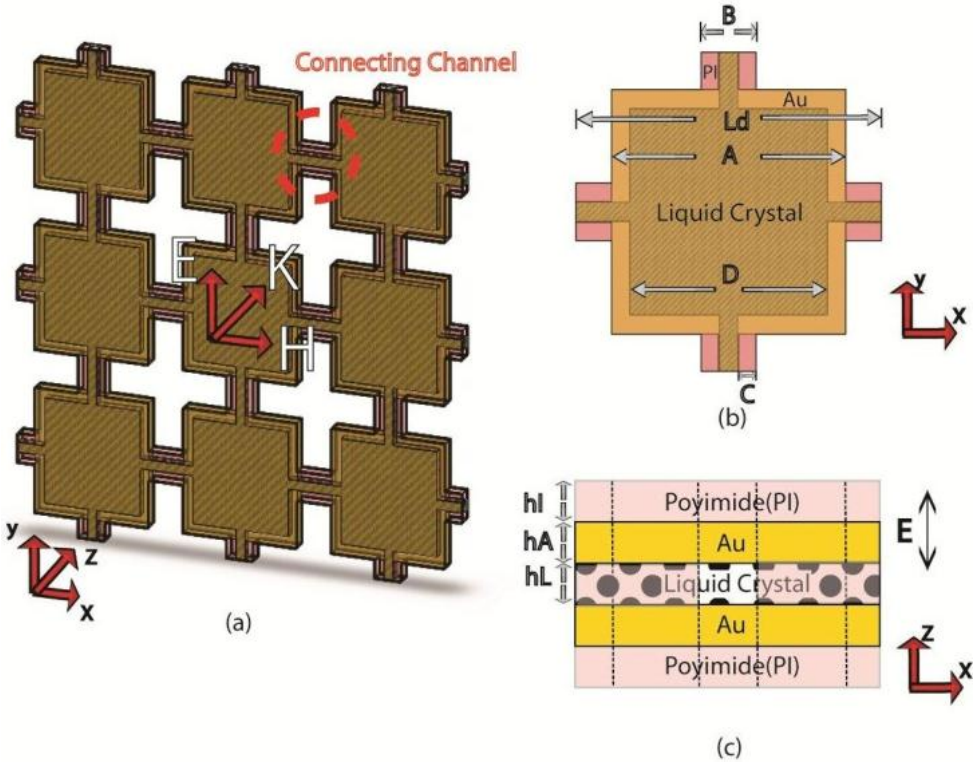

Figure 8: Tunable fishnet structure with liquid crystal filling (a) fishnet array showing that the LC is filled between the top and bottom electrodes which can be turned on and off by applying electric field. The dimension of unit cell is L = 150 μm. The surrounding area of the fishnet structure is open in vacuum (b) top view of unit cell. A=115, μm B= 18 μm, C = 4 μm and D=106 μm (c) side view of fishnet multilayer structure. hI = 4 μm, hA = 0.4μm and hL = 9 μm. The gold adheres to top and bottom polyimide film.

Assume a plane wave incident normally to an infinite fishnet array and the Floquet boundary condition is applied to the unit cell, the wave propagating in this region can be expressed as

$$U(x + Ld,\ y + Ld) = U(x, y)\exp(i\ k\ Ld) \ldots\ldots (4)$$

where U can be electric field or magnetic field k is a complex propagation constant and Ld is the period or the length of a unit cell. In our case, Ld is 150 μm.

The model is being investigated using a finite element frequency domain method. The permittivity of gold is set up based on the Drude dispersion model expressed as

$$\varepsilon = 1 - \frac{{\omega_p}^2}{(\omega^2 + i\,\omega\,\gamma)} \ldots\ldots(5)$$

where ω_p is the plasmon frequency which $\omega_p = 1.37 \times 10^{16}\ s^{-1}$ and γ is the collision frequency which $\gamma = 4.05 \times 10^{13}\ s^{-1}$. Drude dispersion model is a good approximation of metal permittivity in near optical range [41]. The refractive index of liquid crystal follows the property of 5CB obtained from Reference [40] where n_o = 1.55 and n_e = 1.65. The index of polyimide (PI) n = 1.92 in THz range is obtained from a terahertz time domain spectroscopy [42].

3.1.1. Refractive index retrieving algorithm

The complex refractive index *n* and the impedance *z* are retrieved from transmission *S*21 and reflection *S*11 coefficients [38, 43-45] using following equations

$$n\,k\,L_z = \pm\cos^{-1}\frac{1 - S11^2 + S21^2}{2\,S21} + 2\,\pi\,m \ldots\ldots(6)$$

$$z = \pm\sqrt{\frac{(1+S11)^2 - S21^2}{(1-S11)^2 - S21^2}} \ldots\ldots(7)$$

where k is the incident wave number, L_z is the unit cell size in the direction of wave propagation. The imaginary part of refractive index and the impedance can be unambiguously defined by assuming that the effective material is lossy and passive yielding

$$n'' > 0 \ldots\ldots(8)$$

$$z' > 0 \ldots\ldots(9)$$

where n'' is the imaginary part of complex refractive index and z' is the real part of complex impedance. Eq.8 uniquely defines the $\pm$ sign in eq. 6 and eq. 9 defines $\pm$ sign in eq. 7. However, the real part of refractive index (n') is still complicated by the branch index m in eq. 6. Previous technique used to define the m of split ring resonator (SRR) is by comparing SRR with different number of layers and assuming refractive index is not function of layers [43]. The above technique can find the matching refractive index from SRR with different layers. Thus, m can be uniquely defined. However, the refractive index of fishnet metamaterial is function of layers due to the strong coupling effect between closely spaced fishnet layers [19, 46]. Thus, the material properties of SLFM and multilayer fishnet metamaterial (MLFM) should be considered different unless the separation between layers is large enough [19, 47]. In such case, m becomes ambiguous again.

In 3.1.2 and 3.1.3, Chen's algorithm [38] is applied to study the material properties consistency between SLFM and double layer fishnet metamaterial (DLFM) with consideration of the reference plane effect.

3.1.2. Defining reference plane of metamaterial

Refractive index retrieving method of metamaterial introduced above is based on transmission and reflection coefficients, which are accompanied by setting two observing reference planes, one for transmission and the other for reflection. Reference planes where transmission and reflection are measured define the effective material boundaries. The reference planes are usually set on the physical boundaries of a material. However, metamaterial is a resonant device with non-uniform electromagnetic waves near physical boundaries. Thus, how to define the material boundaries becomes important.

The reference planes for regular split ring resonator can be found near the physical boundaries of a unit cell [38]. However, the reference planes of fishnet metamaterial is not clearly defined or discussed previously [19, 20, 39]. To find the reference planes, Chen's method is employed, based on impedance matching between different layers of metamaterial [38]. To be specific, impedance of TFMM with x layers and $(x-1)$ layers must be matched where x is an arbitrary number of layers. The above criterion is based

on the concept that effective refractive index of TFMM is homogeneous so that x layers and $(x-1)$ layers should have the same material properties. The equation of finding the impedance difference of TFMM with x layers and $(x-1)$ layers is shown below

$$\Delta Z_f(L1,L3) = \frac{1}{N_f}\sum_{i=1}^{N_f}\frac{|z_x(f_i,L1,L3)-z_{x-1}(f_i,L1,L3)|}{max\{|z_x(f_i,L1,L3)|,|z_{x-1}(f_i,L1,L3)|\}} \quad \text{.....(10)}$$

where $\Delta Z_f(L1,L3)$ is the impedance difference between x and $(x-1)$ layer. L1 and L3 is the distance to reference planes for calculating transmission and reflection coefficients. We set two coordinate systems for reference planes at LHS and RHS of TFMM as shown in Figure 9. Reference planes are swept from 0 to 75 μm for all possible combination of L1 and L3. L1, L3 and thickness of TFMM together define the equivalent material thickness. In eq. 10, $z_x(f_i,L1,L3)$ means that impedance z_x from eq. 7 is calculated at specific frequency f_i and the distance from reference planes set at L1 and L3. The local impedance difference $z_x - z_{x-1}$ is normalized to local maximum. Then, the summation of local impedance differences over the entire frequency domain is then averaged by total number of samples which is N_f in eq. 10.

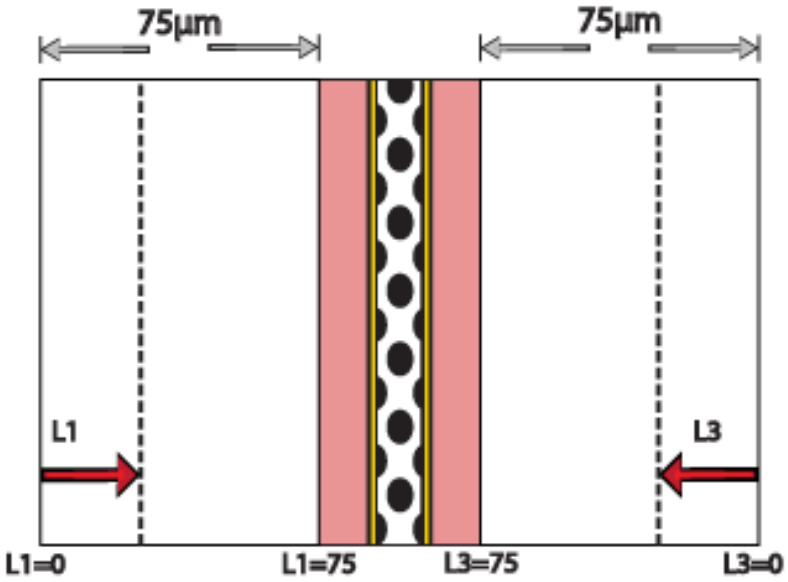

Figure 9: Distance to reference planes for calculating the effective refractive index and impedance. L1 and L3 coordinate systems for reference planes (dashed line) are

set at LHS and RHS of TFMM. Plane wave is excited at L1=0 and the reference plane is swept from 0~75 μm to find the minimum impedance difference. The right reference plane is used to calculate the S parameter and determine the equivalent material thickness.

3.1.3. Impedance matching of SLFM and DLFM

The algorithm introduced in 3.1.2 for calculating minimum impedance difference between m layers and $(m-1)$ layers is applied to SLFM and DLFM to show that the impedance of SLFM is different than DLFM. Figure 10 shows the contour plot of impedance difference between SLFM and DLFM with respect to L1 and L3 from 0 to 75μm. The minimum impedance is found at L=L1=L3=45 μm

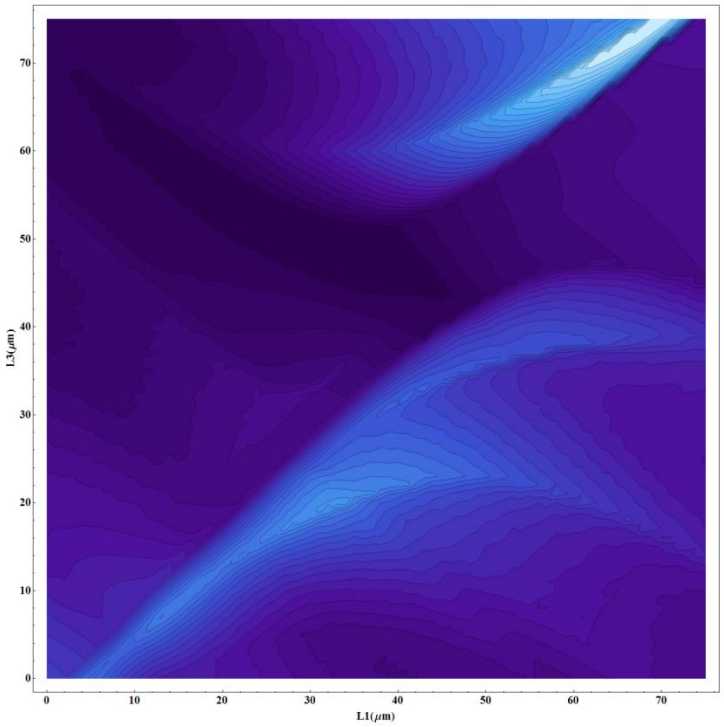

Figure 10: Contour plot of impedance difference between SLFM and DLFM with respect to reference planes set in L1 and L3 coordinate system.

Impedances of SLFM and DLFM are shown in Figure 11. Even though the minimum impedance difference is found, the impedance of SLFM is still significantly different than

DLFM at frequency from 0.8 THz to 1 THz, where the major resonance occurs. This proves that there are no optimal reference planes for both SLFM and DLFM, and that the impedances of SLFM and DLFM are intrinsically different.

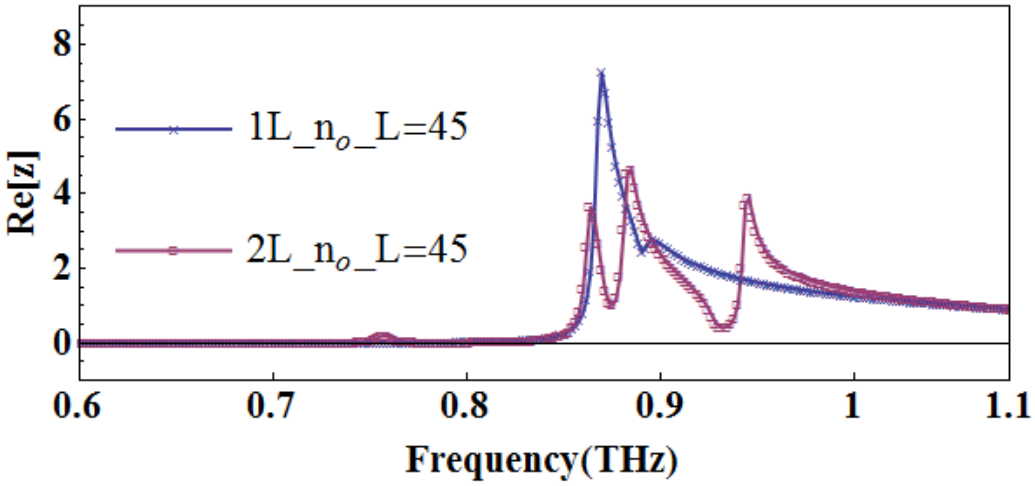

Figure 11: Impedance of SLFM and DLFM with reference planes set at L=L1=L3=45μ*m*

Refractive indices for SLFM are shown in Figure 12 with different reference planes set at L=75, 65, 55 and 45 μm to indicate the effect of reference plane variation on the value of the retrieved refractive indices. Clearly, if reference planes are closer to the physical material boundaries, the domain inside the reference planes include less vacuum area, resulting in a larger negative refractive index for the SLFM case. On the other hand, if the reference planes move away from the physical material boundaries, the effect of negative refractive index will be averaged out by the vacuum area. Without comparing different layers of fishnet metamaterial, there is no specific criterion in determining the reference planes (effective material boundaries). Thus, the effective material boundaries of SLFM are difficult to be defined.

Chen's algorithm [38] provides the physical means to find the effective material boundaries of SRR. If the reference planes, where the reflected and transmitted waves from the SRR behave like plane waves, can be found, then these reference planes should represent the effective material boundaries of SRR. However, in our research, the

reference planes of SLFM are not defined by above approach, but are arbitrarily defined at the physical material boundaries.

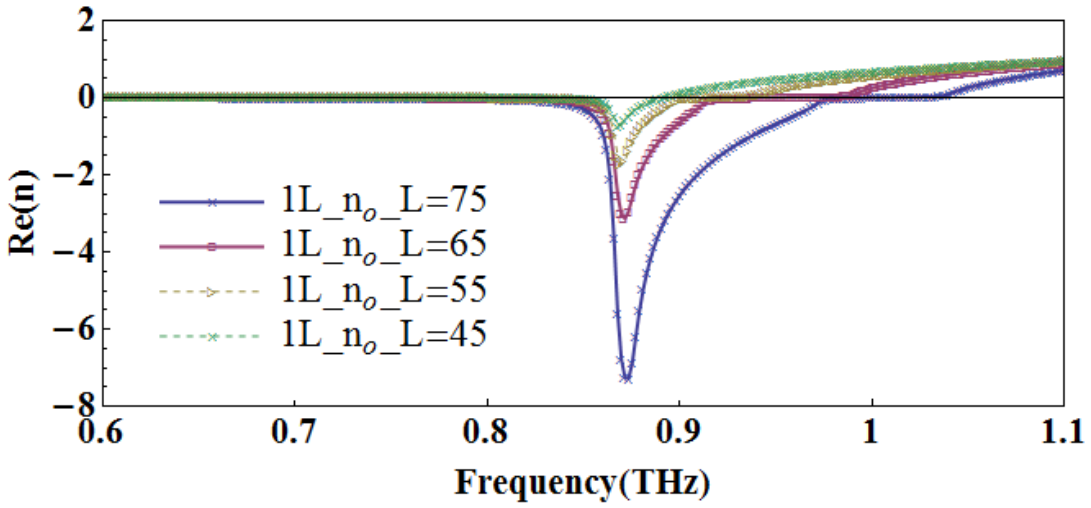

Figure 12: Refractive index of SLFM with reference planes set at L=L1=L3=75, 65, 55 and 45μm.

3.1.4. Determination of n' branch and anti-resonance

We have shown that the material properties of SLFM and DLFM are intrinsically different meaning that we could not compare SLFM and DLFM to solve ambiguous *m*. Thus, a new approach should be considered. The assumption that the metamaterial is lossy, indicating simultaneously decaying electric and magnetic fields, resulting in continuity of simultaneous positive imaginary permittivity (ε'') and permeability(μ''). The above assumption can be used to further determine *m*, which can be expressed in terms of n and z [38]

$$|n'z''| \leq n''z' \quad \ldots\ldots(11)$$

where z'' is the imaginary part of impedance. Eq. 11 removes the ambiguous n' in the off-resonant band but cuts off all branches of n'near resonant band (dashed box in Figure 13a) because of negative ε'' and positive μ'' (dashed box in Figure 13b), which do not

satisfy eq. 11. The region where negative ε'' and positive μ'' occur is called anti-resonance [38], which will be explained in next paragraph. Despite of anti-resonant phenomenon, we apply eq. 11, assuming continuity of simultaneously positive ε'' and μ'', to determine the branch index (m) in the off-resonant region and retain n' from the selected m near the resonant band where anti-resonance occurs.

Anti-resonant phenomenon means that near the resonant band, negative imaginary permittivity ($\varepsilon^{"}$), increased electric field, violate the assumption (eq. 11) that the material is lossy, electric field should decay, and its imaginary permittivity should be positive, yielding an undetermined real part of refractive index (dashed box in Figure 13a). However, anti-resonant behavior does not necessary violate energy conservation since the power dissipation per unit volume [38] is a function of both imaginary permittivity and imaginary permeability ($\mu^{"}$) expressed as

$$\frac{\omega\,\varepsilon_o\,\varepsilon^{"}}{2}|\bar{E}|^2+\frac{\omega\,\mu_o\,\mu^{"}}{2}|\bar{H}|^2\ldots\ldots(12)$$

where ω is the operating frequency, E is the electric field and H is the magnetic field. ε_o and μ_o are permittivity and permeability in vacuum.

The retrieved n', ε'' and μ'' of SLFM with no polyimide layer is shown in Figure 13. Below the anti-resonant band (0.85THz~0.91THz), where ε'' is negative, the higher order branches will be removed by eq.11 leaving only n' with m=0 (Figure 13a). μ'' and ε'' (Figure 13b) have opposing signs near the resonant band, showing the anti-resonant behavior similar to SRR [48].

Furthermore, a study of validity of effective medium theory was conducted to show that anti-resonance near resonant region does not fail the retrieved results. Since the effective medium theory is based on the assumption that wavelength is much longer than unit cell size. The increasing amplitude of n', near resonant band, can shorten the wavelength and makes it comparable to the unit cell size, which fails the effective medium assumption. In order to understand how n' affects wavelength, we calculate the approximate allowable n'_{allow}, assuming the wavelength inside SLFM should be larger than twice the unit cell size

$$|n'_{allow}| \leq \frac{c}{2fL_z} \quad \ldots\ldots(13)$$

where f is the operating frequency and c is the speed of light. In the case of SLFM with no polyimide layer, L_z is 9.8 µm. At resonance, (0.87THz), the retrieved $|n'|$ ~ 15 (Figure 13a) does not exceed $|n'_{allow}|$ = 17.35, meaning that effective medium theory is valid which is in agreement with the result from previous work on SRR [48].

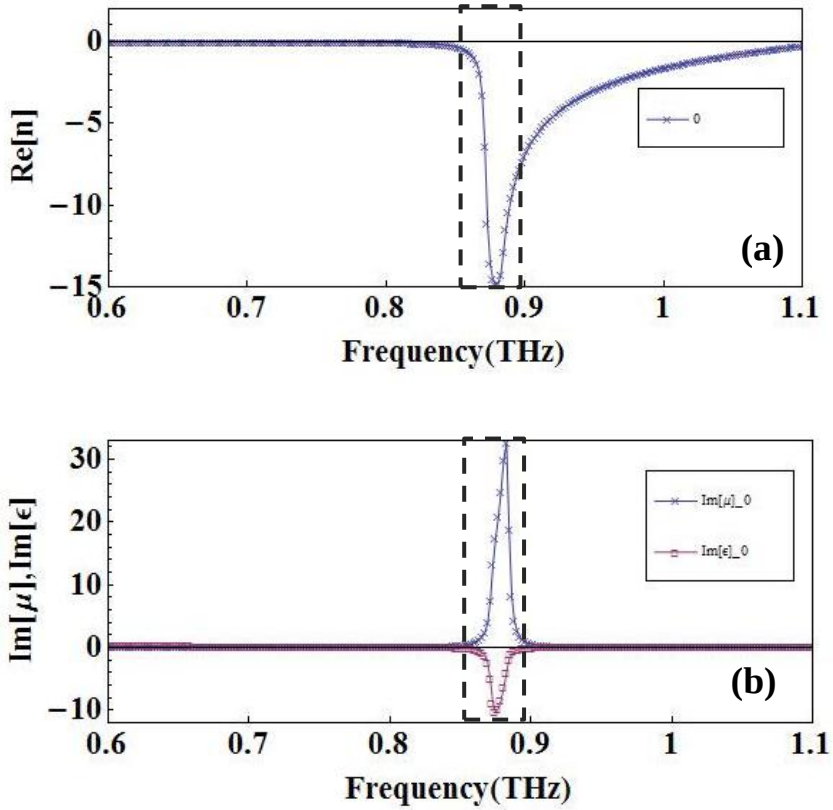

Figure 13: (a) $n^{'}$ of SLFM with hI=0 (b) $\mu^{''}$ and $\varepsilon^{''}$ of SLFM where anti-resonant region is shown inside the dashed region.

3.1.5. Effect of polyimide thickness on anti-resonance

Polyimide (PI) layers with different thicknesses were added on the fishnet metamaterial (Figure 8c) to study the relationships between n', ε" and µ" near the resonant band. The reference planes for calculating transmission and reflection are set on the very

top and bottom of each PI layer. The amplitude of retrieved negative refractive index (b) decreases as the thickness of the PI layer increases. The | n' | at resonant frequency of SLFM with PI thickness of 8 µm, 16 µm, and 20 µm are 5, 0.9, and 1 respectively. Based on the results, the refractive indices are all smaller than $|n'_{allow}|$, which validate the assumption that wavelength inside SLFM is larger than twice the unit cell size in the direction of propagation. The anti-resonant band where ε'' is negative (Figure 14d) accompanied by positive μ'' (Figure 14c) and negative n' (Figure 14b) also decrease when the PI thickness increases. When PI layer thickness becomes 20 µm, ε'' and n' become all positive near resonant band. This result indicates that the anti-resonant behavior is inherent to SLFM and cannot be removed by changing the material boundaries (reference planes) if one wants to obtain a negative refractive index.

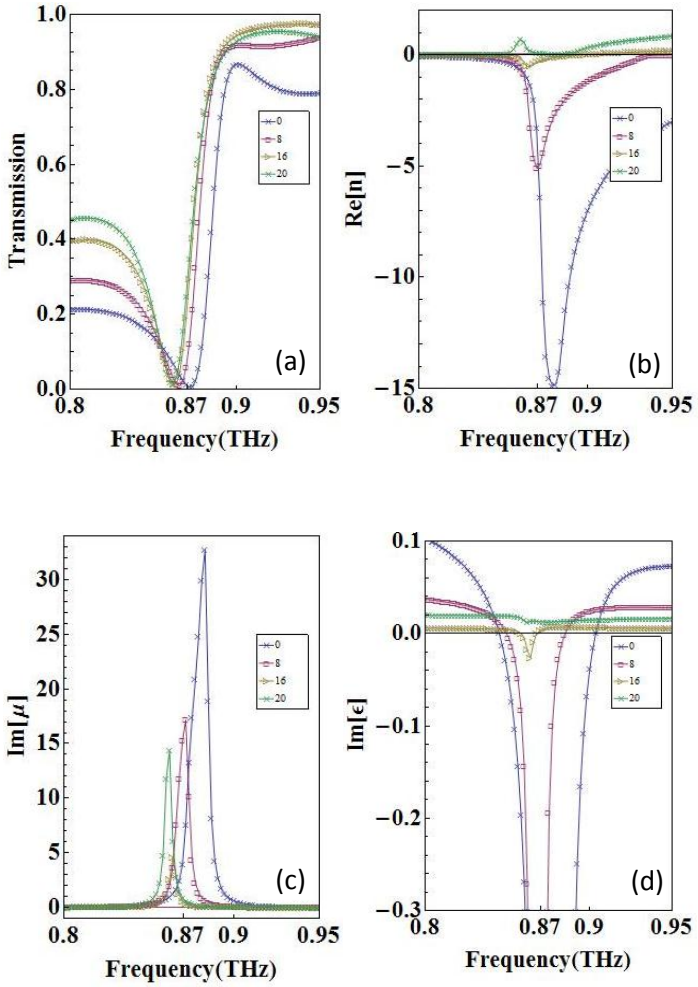

Figure 14: Retrieved parameters of SLFM with different PI thickness from 0, 8, 16 to 20 µm (a) transmission (b) $n^{'}$ (c) $\mu^{''}$ (d) $\varepsilon^{''}$

3.2. Tunability study of single layer fishnet metamaterial (SLFM)

To understand how much refractive index can be tuned when liquid crystal is infiltrated between two fishnet electrodes, the refractive indices of SLFM with liquid crystal set at ordinary state (n_o =1.55) and extra ordinary state (n_e =1.65) are studied (Figure 15). The refractive index birefringence of liquid crystal (5CB) is obtained from the literature[40] at around 1 THz. The resonant frequency shifts observed from transmission dips, reflection dips and refractive index dips of n_o and n_e states are shown in Table 1. Transmission dip shifts from 0.93 THz to 0.89 THz when liquid crystal is turned from ordinary to extra ordinary state giving total shift about 0.04THz. Similar to the tunable range of transmission dip, frequency shifts of reflection dips and refractive index dips are 0.06 and 0.05 THz respectively.

	Transmission dip	Reflection dip	Refractive index dip
Δf	0.04 (0.93 to 0.89 THz)	0.06 (0.97 to 9.91 THz)	0.05 (0.95 to 0.9 THz)

Table 1: Resonant frequency shift of SLFM with liquid crystal tuned from ordinary state (n_o =1.55) to extra-ordinary state (n_e =1.65).

The tunable range of refractive index is the most important parameter for changing beam steering angle. Thus, we investigate the tunable range at the frequencies where two refractive index dips and maximum figure of merit (FOM=$\frac{-Re(n)}{Im(n)}$) occur (Table 2). The observed maximum refractive index change (Δn) is 12 at 0.95THz. However, the corresponding transmission is small (0.25) and the figure of merit is also small (4) at ordinary state. The most practical operation frequency is around 1THz where the FOM change from 26 to 32. Transmission is maintained near 0.86 and the refractive index change is 2.5.

	f=1THz	f=0.95THz	f=0.9THz
Δn	2.5 (-3 to -0.5)	12 (-13 to -1)	-6 (0 to -6)
ΔT	-0.04 (0.86 to 0.82)	0.55 (0.25 to 0.8)	-0.05 (0.3 to 0.25)
ΔFOM	6 (26 to 32)	26 (4 to 30)	0 (0 to 0)

Table 2: Variation of refractive index, transmission and figure of merit at different operating frequencies.

A RLC circuit model in eq. 14 can be used to explain the physical meaning behind the resonant dip shift [36]

$$\omega_m \propto \sqrt{\frac{1}{L_m C_m}} \quad \text{.....(14)}$$

where ω_m is the magnetic resonant frequency, L_m is the inductance and C_m is the capacitance of SLFM. In eq. 14, the capacitance between top and bottom fishnet electrodes is tuned by the dielectric constant of the liquid crystal (proportional to the change in the refractive index of the material from n_o to n_e) which controls the magnetic resonance [35, 49]. Using the RLC circuit concept, enlarging the dielectric constant from n_o to n_e causes the capacitance to increase. Thus the resonant frequency will decrease.

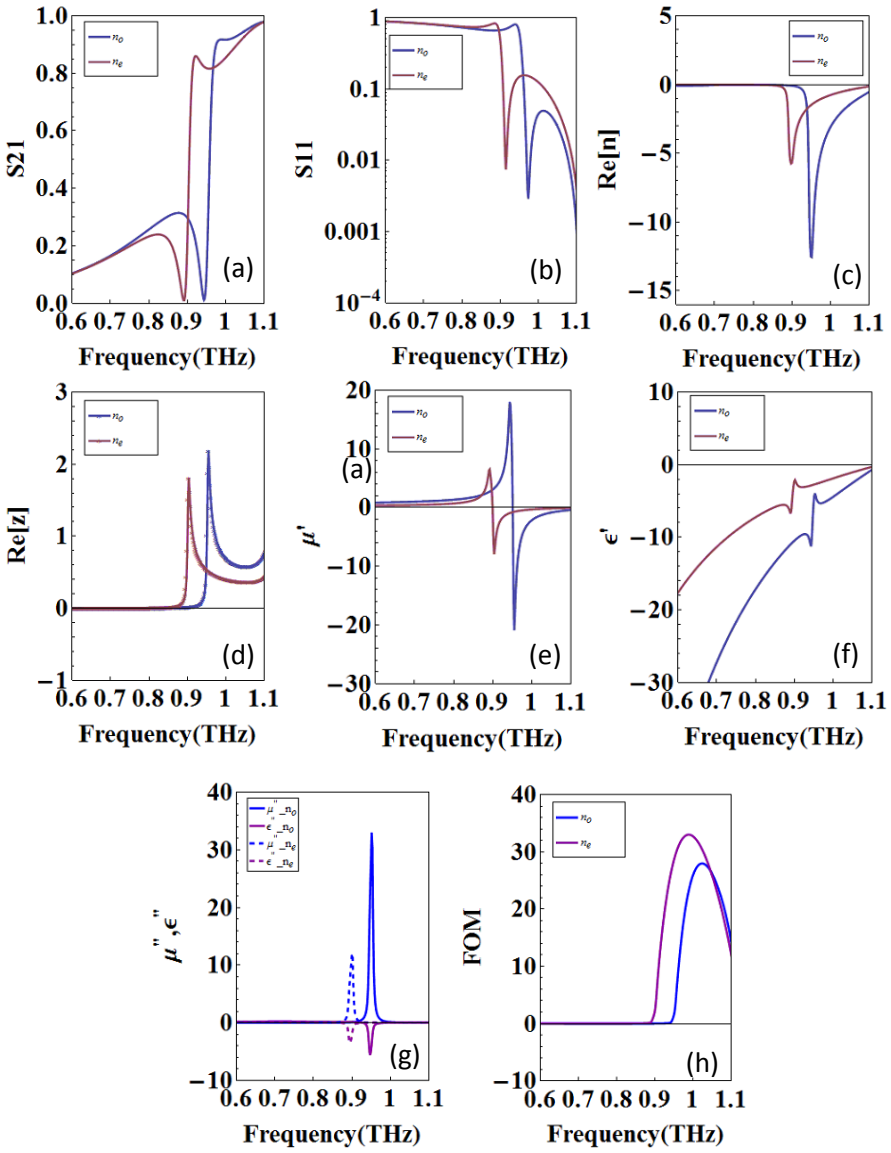

Figure 15: Tunability of SLFM with liquid crystal (5BC) set at ordinary state (n_o =1.55) and (n_e =1.65) (a-b) transmission and reflection (c-d) refractive index and impedance (e-f) real part of permeability and permittivity (g) imaginary part of permeability and permittivity. (h) FOM ($-Re(n)/Im(n)$)

These preliminary results are based on liquid crystal where its material properties in THz region that can be found in the literature [40]. However, since the PDLC will be used in our research and the material properties of PDLC depend on the droplet size

which is determined by fabrication process. Thus, we will focus on fabricating the PDLC-TFMM and direct apply the algorithm developed in chapter 3 to PDLC-TFMM.

3.3. Modeling of multilayer fishnet metamaterial (MLFM)

Based on the fact that single layered fishnet metamaterial (SLFM) does not generally possess the same material properties as MLFM [19], it is difficult to compare SLFM with double layered fishnet metamaterial (DLFM) and find the reference planes where impedances are matched. However, MLFM is a good candidate to be studied because the refractive indices of MLFMs converge. To insure a proper reference planes for MLFM. We first set the reference planes at the very top and bottom fishnet electrodes and add more layers until the magnitude of both transmission curves become relatively convergent. Once convergent layers of fishnet metamaterial are found, we start to move the reference planes away from the two electrodes until the minimum impedance difference between convergent layers is found.

After running the optimization, we found the transmission curves relatively convergent around 8 and 9 layers. The evolution of transmission curve of MLFM with 1, 3, 5, 8 and 9 layers are shown in Figure 16. The liquid crystal sandwiched in MLFM is set in ordinary state. The convergent layer is determined by looking at relative difference of transmission between fishnet metamaterial with x layers and $(x-1)$ layers where x is an arbitrary number of layers. 8 and 9 layers MLFM are considered close in our simulation.

The contour plot in (Figure 17b-c) shows the impedance difference between 8 and 9 layers versus the position of reference planes in L1 and L3 coordinate systems. Impedance differences for both n_o and n_e cases were investigated and the minimum impedance differences for n_o and n_e cases are found at L=24 μm and L=35 μm respectively where L=L1=L3. Since reference planes represent the effective material boundaries, the results indicate that the equivalent thicknesses of fishnet metamaterial are different for n_o and n_e cases. For the n_e case, the large dielectric constant within the metamaterial results in stronger resonance and thicker effective material boundaries. The impedances of n_o and n_e cases calculated using L= 35 μm and 24 μm respectively are shown in Figure 17d.

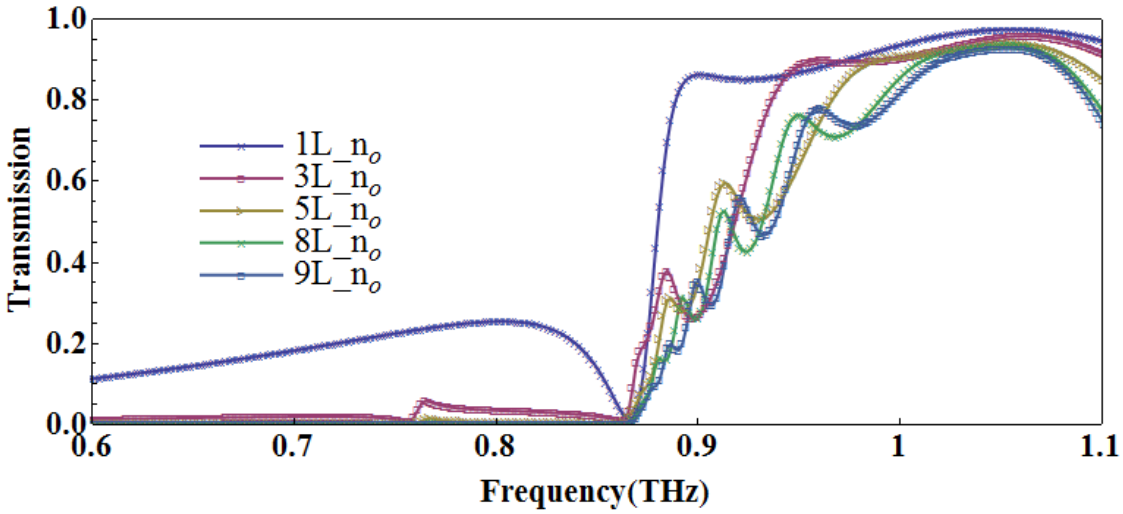

Figure 16: Transmission of fishnet metamaterial with different layers for liquid crystal set in ordinary state (n_o). Only one resonant dip of single layered fishnet metamaterial (SLFM) is found. However, MLFM shows more resonant dips meaning that more resonant modes are excited.

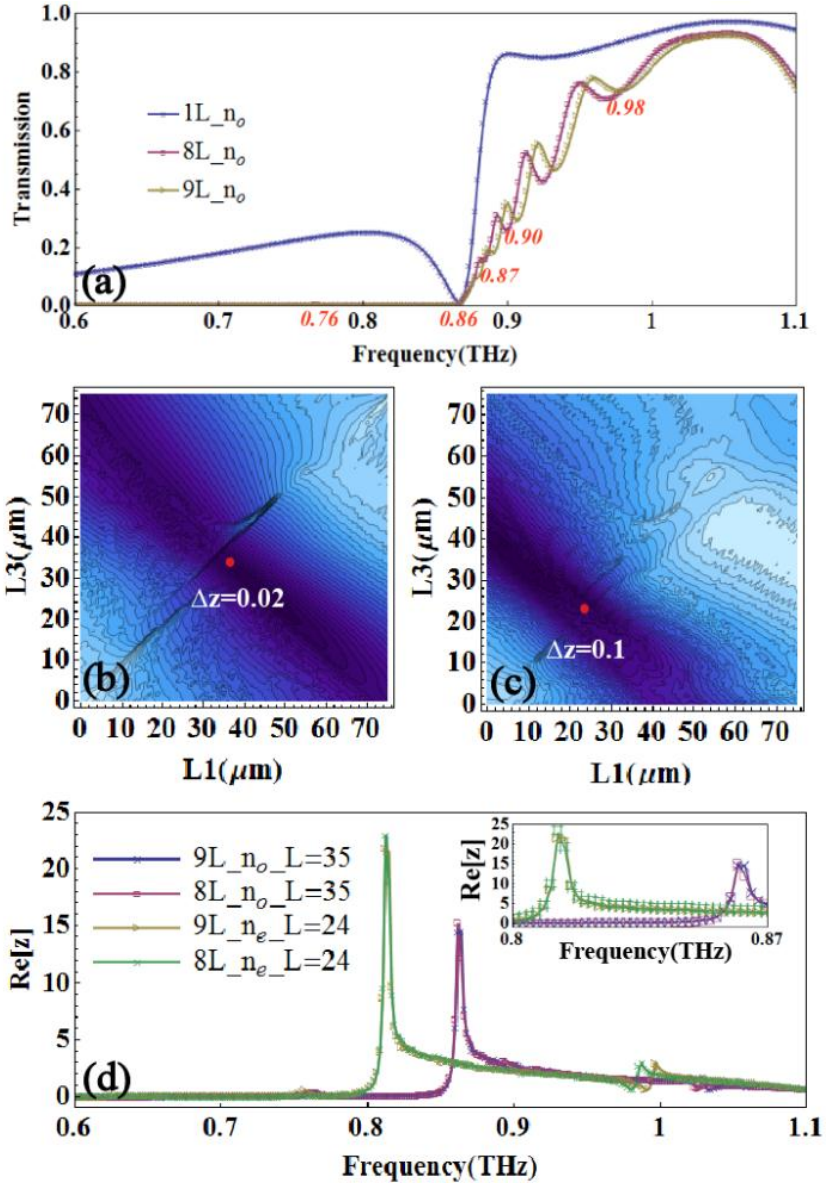

Figure 17: (a) Transmission of 1, 8 and 9 layers fishnet metamaterial for liquid crystal set at ordinary state (n_o case). (b) and (c) are the contour plots of impedance differences between 9 and 8 layer fishnet metamaterial respect to the position of reference planes at L1 and L3 coordinate systems. The minimum impedance differences occurs at L1=L3=35 μm and L1=L3=24 μm for for n_o and n_e cases. (d) Impedances of 8 and 9 layer for n_o and n_e cases show that impedances are matched between 8 and 9 layers when optimal reference planes are found.

Transmission curve in Figure 17a indicates that only one resonant dip at 0.86 THz occurs in SLFM case, However, Five resonant dips at 0.76, 0.86,0.87, 0.90 and 0.98 THz that generate sign change of refractive indices (Figure 18) can be found in 8 and 9 layers fishnet metamaterials. The discontinued refractive indices might indicate that the retrieving method fails because the refractive indices goes beyond the n'_{allow} forcing the selection of $\pm$ sign in eq. 6 to be opposite. However, more study is required to confirm this assumption.

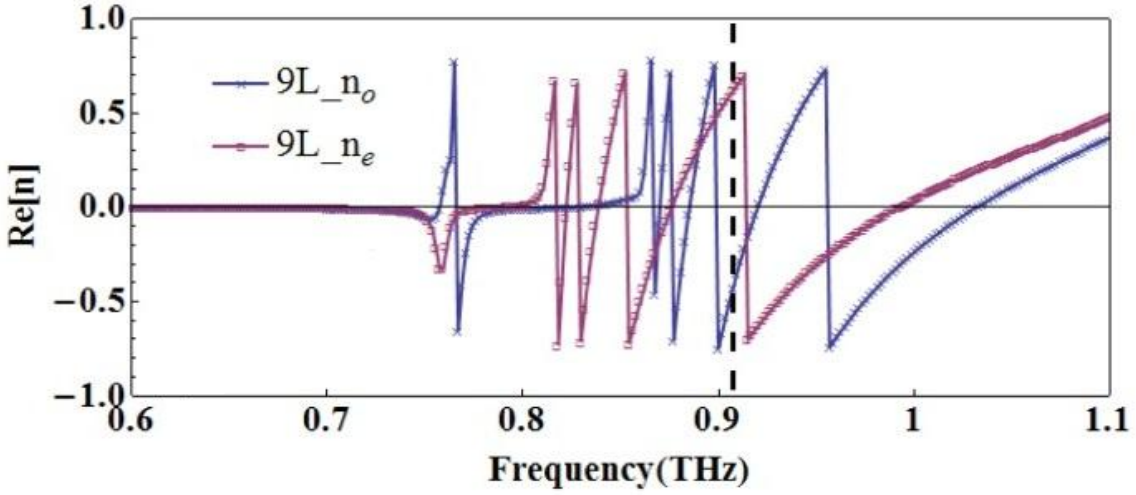

Figure 18: Refractive indices of 9 layer TFMM with PDLC set at n_o and n_e states where n_o =1.55 and n_e =1.65. Five discontinued refractive index points from positive to negative are found at both cases.

Chapter 4

Characterization of tunable fishnet metamaterial (TFMM) by terahertz time domain spectroscopy (THz-TDS)

4.1 Introduction to terahertz time domain spectroscopy (THz-TDS)

In this section, we will first describe how to use terahertz time domain spectroscopy (THz-TDS) to characterize the properties of materials in THz range. The principle of THz-TDS is based on photoconductive THz generation and detection technique. To generate THz pulses, the emitter of the system contains a THz antenna and femtosecond (FS) laser (Figure 19). The periodic FS laser pulses will first impinge on a photoconductive antenna and induce a transient current. Consequently, this transient current only exists in a femtosecond time scale, generating radiation in the THz range. The generated THz radiation also has same repetition rate as the impinging FS laser. This conversion between FS laser pulse and transient current occurs in a biased semiconductor built into the photoconductive antenna. With sufficient energy, the laser pulse can excite electrons in semiconductor to cross into the conducting band [50]. These free charges are then accelerated by the semiconductor's biasing field. Thus, the FS laser serves as a photo switch or a gate signal to turn semiconductor on and off.

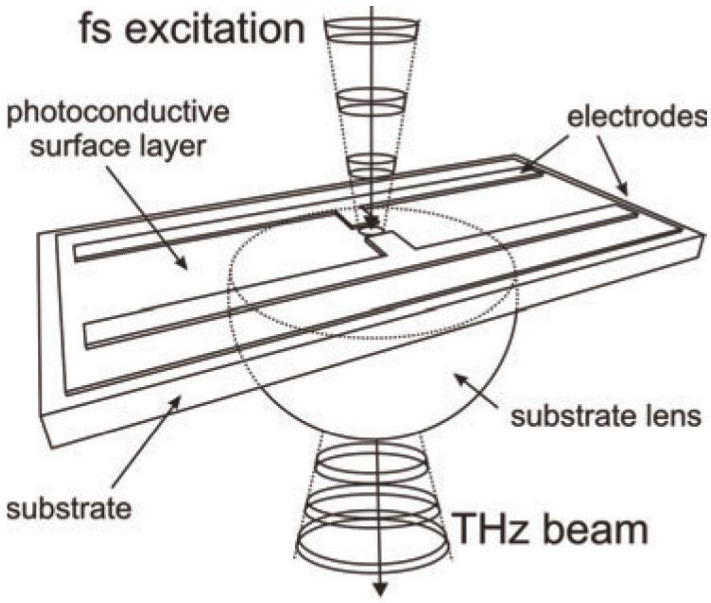

Figure 19: Photoconductive antenna radiates a THz field when a femtosecond laser impinges on the semiconductor and bridges the electrodes of the dipole antenna[50]

The detection of THz field is similar to THz emitter, based on the concept of photoconductive sampling. The detector is composed of a semiconductor and a THz antenna; however, the bias that drives the free charges is not supplied by external field but by the impinging THz radiation. The FS laser then serves as the sampling signal (Figure 20).

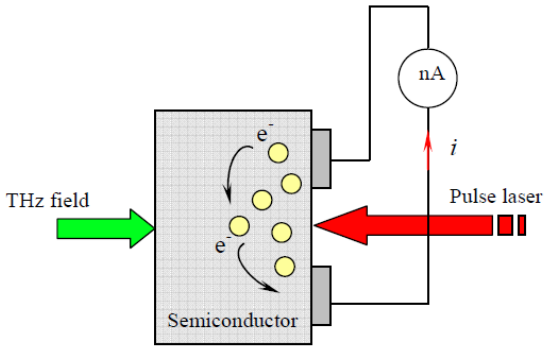

Figure 20: Working principle of THz detector[51]. THz radiation impinging on the semiconductor creates a bias voltage. However, without free charges generated by pulse laser, there will be no current.

Similar to converting an analog signal to digital signal, reconstructing a THz waveform in the time domain requires photoconductive sampling of the field. Sampling the THz field requires the FS laser to precisely scan over a given time period. This can be accomplished by using the time delay (Δt) between the arriving THz radiation and the FS laser pulse. Without changing Δt, the probing pulse (FS laser) will measure a single time spot of THz field, making detection impossible. The detected THz field can be averaged because the impinging THz radiation and probing pulse are both periodic. Figure 21 illustrates the concept of using time delay to detect THz field.

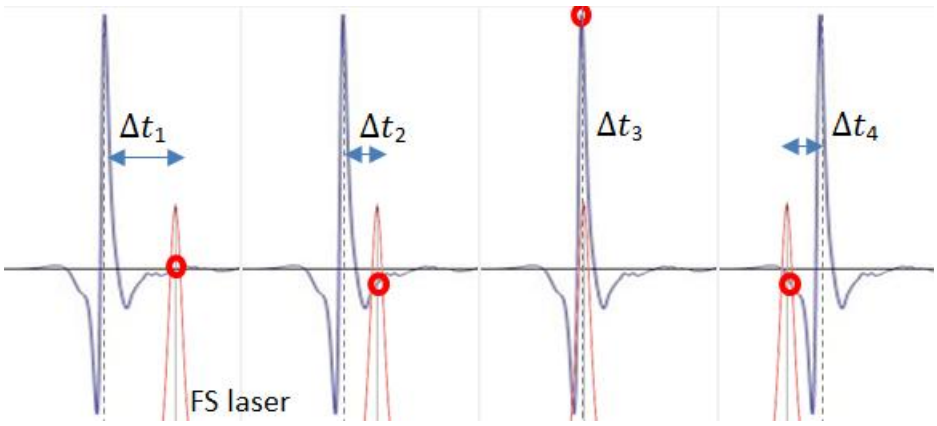

Figure 21: Photoconductive sampling of THz field by femtosecond laser pulses. Adjusting the time delay between impinging THz radiation and FS laser can provide THz field information at different times.

The detected transient photoconductive current is the convolution of the impinging THz field and transient photoconductivity induced by the FS pulse, as shown in the following equation.

$$J_{total}(t) = \int_0^{+\infty} \sigma_s\,(t - \Delta t) E_{THz}(\Delta t) d\,\Delta t \quad \text{.....} (15)$$

where J_{total} is the total transient current detected, σ_s is the surface conductivity of the semiconductor induced by probing signal, E_{THz} is the detected THz field, and Δt is the time delay between the probing pulse and E_{THz} [52].

4.1.1 EKSPLA THz-TDS system

The THZ-TDS system used in our research is EKSPLA. EKSPLA THz-TDS is a system based on photoconductive THz generation and detection technique. The femtosecond (FS) laser of an EKSPLA system is a Ti-Sapphire laser with 50~150 femtosecond pulses and an 80 MHz repetition rate. The output power is 50 mW and the center wavelength of the pumping laser is 800nm. During operation, the FS laser first splits into a pumping beam and a probe beam. The pumping beam goes through the fast delay line (HLR1 in Figure 22) to adjust the optical path before reaching the emitter, while the optical path of the probing beam is adjusted by the slow delay line (HLR2 in Figure 22). The slow delay line is used for large time delay calibration while fast delay line is for quick adjustment of time delay (Figure 22-23). Both effects of the fast and slow delay lines combined will result in time delay between pumping beam and probing beam.

The emitter is a LTG (low-temperature grown) GaAs-based photoconductive antenna with an emitting power of 5μW for a 50mW FS laser impinging on the semiconductor. The dimension of the semiconductor is 5*1.5mm with 40V maximum bias voltage. The emitted THz radiation is collimated by a high resistance (resistivity>10000 ohm/cm) silicon collimator. The THz detector is also a LTG GaAs-based photoconductive antenna with the same specifications as the emitter. However, no bias voltage is provided to the detector.

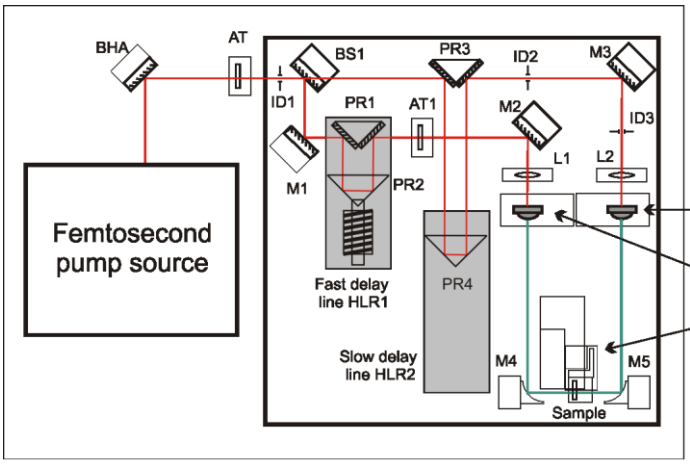

Figure 22: Illustration of EKSPLA system diagram, BHA: beam high adapter, M: mirror, BS: beam splitter, PR: Prism, HLR: Hollow retro reflector (mounted on fast moving stage), L: Lens and DSP: digital signal processing

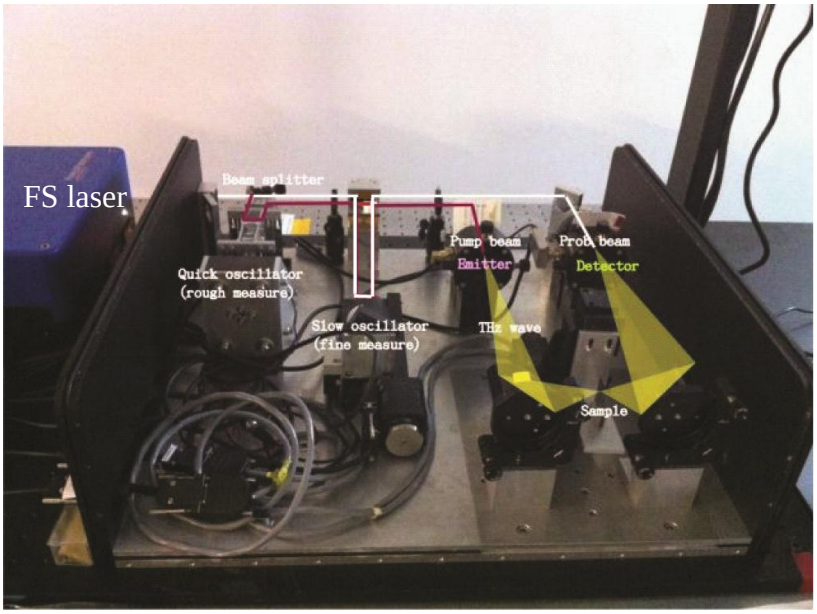

Figure 23: EKSPLA system, the FS laser goes through the BHA and is then split into a pumping beam (red, fast delay line) and a probing beam (white, slow delay line). The pumping beam impinges on the emitter while the probing beam (white) impinges on detector. The THz radiation (yellow) is focused on the sample by parabolic lens.

4.1.2 Characterization of refractive index from THz-TDS

The temporal terahertz pulses transmitted or reflected by a material can be used to extract material properties in THz region, such as the refractive index. Fields in the time domain are first converted by the Fast Fourier Transform to obtain frequency information. Then the fields are normalized to reference fields to calculate transmissions and reflections. However, calculating the refractive index from transmission and reflection requires two independent setups of measurement modes (transmission and reflection). Thus, calculating the refractive index of a material from transmission is usually favored. The transmission (with normal incidence) can be written in the following form [53]

$$T(\omega) = \frac{E_{sample}}{E_{ref.}} = \frac{4\, n_{ref.} n_{sample}}{\left(n_{sample}+n_{ref}\right)^2} e^{-\frac{i\,\omega\, d\left(n_{sample}-n_{ref}\right)}{c}} \times FP(\omega) \ldots\ldots (16)$$

where $T(\omega)$ is the transmission coefficient calculated by normalizing electric field of the sample (E_{sample}) to reference field ($E_{ref.}$), $n_{ref.}$ and n_{sample} are the refractive indexes of the reference and sample, d is the sample thickness and c is the speed of light. $FP(\omega)$ is the Fabry-Perot coefficient representing the effect of multiple internal reflections inside the sample, as shown in Figure 24. $FP(\omega)$ of the first three transmitted modes can be written in the following form:

$$FP(\omega) = 1 + \sum_{k=1}^{2} \left(r_{10}^2\, exp[\frac{i\, n_{sample}\, \omega\, d}{c}](\omega, d)\right)^k \ldots\ldots (17)$$

where r_{10} is the reflection coefficient of first reflection from sample back to reference. The multiple internal reflections induce more than one transmission mode. Higher modes prevent retrieving the refractive index from a single transmission[54] due to the $FP(\omega)$ [53].

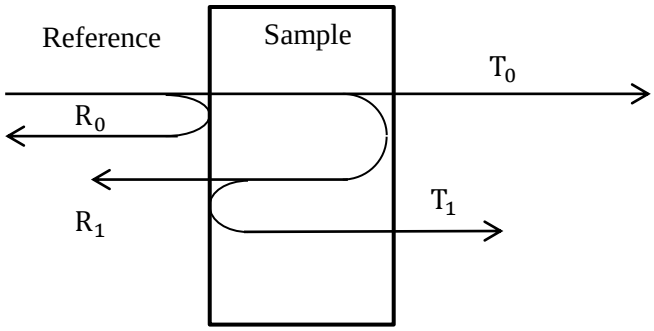

Figure 24: Multiple transmissions and reflections. T_0 and R_0 are first transmission and reflection modes. $T_1$and R_1 are second modes.

When the sample thickness is large enough to a level where the higher modes ($T_1$and R_1 to T_n and R_n) can be clearly separated time domain and removed by a time window (Figure 25), Eq. 16 can be simplified to the following form, because $FP(\omega) = 1$.

$$\boldsymbol{T(\omega)} = \frac{\boldsymbol{E_{sample}}}{\boldsymbol{E_{ref.}}} = \frac{\boldsymbol{4\, n_{ref.} n_{sample}}}{\boldsymbol{(n_{sample}+n_{ref})^2}}\, \boldsymbol{e}^{-\frac{\boldsymbol{i\,\omega\, d(\, n_{sample}-n_{ref})}}{\boldsymbol{c}}} \quad \ldots\ldots(18)$$

If the reference environment is air or nitrogen, then $n_{ref.} \approx 1$, we can further simplify the equation to:

$$\boldsymbol{T(\omega)} = \boldsymbol{Abs[T(\omega)]e^{i(\emptyset_{sample}-\emptyset_{ref})}} = \frac{\boldsymbol{4\, n_{sample}}}{\boldsymbol{(n_{sample}+1)^2}}\, \boldsymbol{e}^{-\frac{\boldsymbol{i\,\omega\, d(\, n_{sample}-1)}}{\boldsymbol{c}}} \quad \ldots\ldots(19)$$

We can write complex form of n_{sample}=$n_s' + i\, n_s''$. If the absorption of the sample is negligible, then we can write real part of the n_{sample} (n_s') in the following form.

$$n_s' = 1 + \frac{(\emptyset_{sample}-\emptyset_{ref})c}{\omega\, d} \quad \ldots\ldots(20)$$

The above equation allows us to retrieve the refractive index by just measuring transmission through a material. This simple technique only works for thick and low absorption materials. For thin samples, retrieving the refractive index still requires two independent transmission and reflection mode measurements (Eq. 6 in 3.1.1)

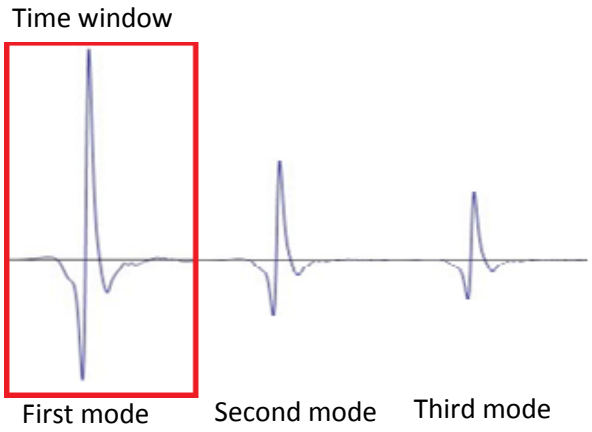

Figure 25: Time-window technique to remove higher modes of THz electric field

The time window technique works only when sample is thick enough to distinguish different transmission and reflection modes. If the sample is too thin, then the higher modes will be hidden inside the first mode. In such a case, two measurement setups[54] are required. The measurement of thin VWR cover glass (180μm) substrate with two setups is shown in Figure 26. The total time period is 40 ps with time resolution 0.01 ps. The signals are individually converted by Fast Fourier Transform (FFT) to the frequency domain (Figure 26c-d). Then the transmission and reflection of the glass is normalized to nitrogen to calculate S21 and S11 (Figure 26e). The S21 and S11 of VWR glass (Figure 27a) are then used in Eq. 6 with sample thickness (L_z) =180μm. The real part of refractive index is around 1.4 (Figure 27b) and imaginary part of refractive index is increasing (0.1 to 0.3) when the frequency increases (0.6 to 1.6 THz). The increasing imaginary refractive index means that the glass substrate becomes more lossy at higher frequencies [55].

The above techniques show how to characterize a thin substrate in THz range from transmission and reflection based on the model developed in 3.1.1. This becomes

important because the metamaterials are too thin and lossy so that characterization from transmission mode is not possible. Furthermore, metamaterials are usually fabricated on substrates, forming composites. Thus, the transmission and reflection measured from a metamaterial on substrate are a combined effect. The aforementioned time-window technique can be used to remove substrate effect.

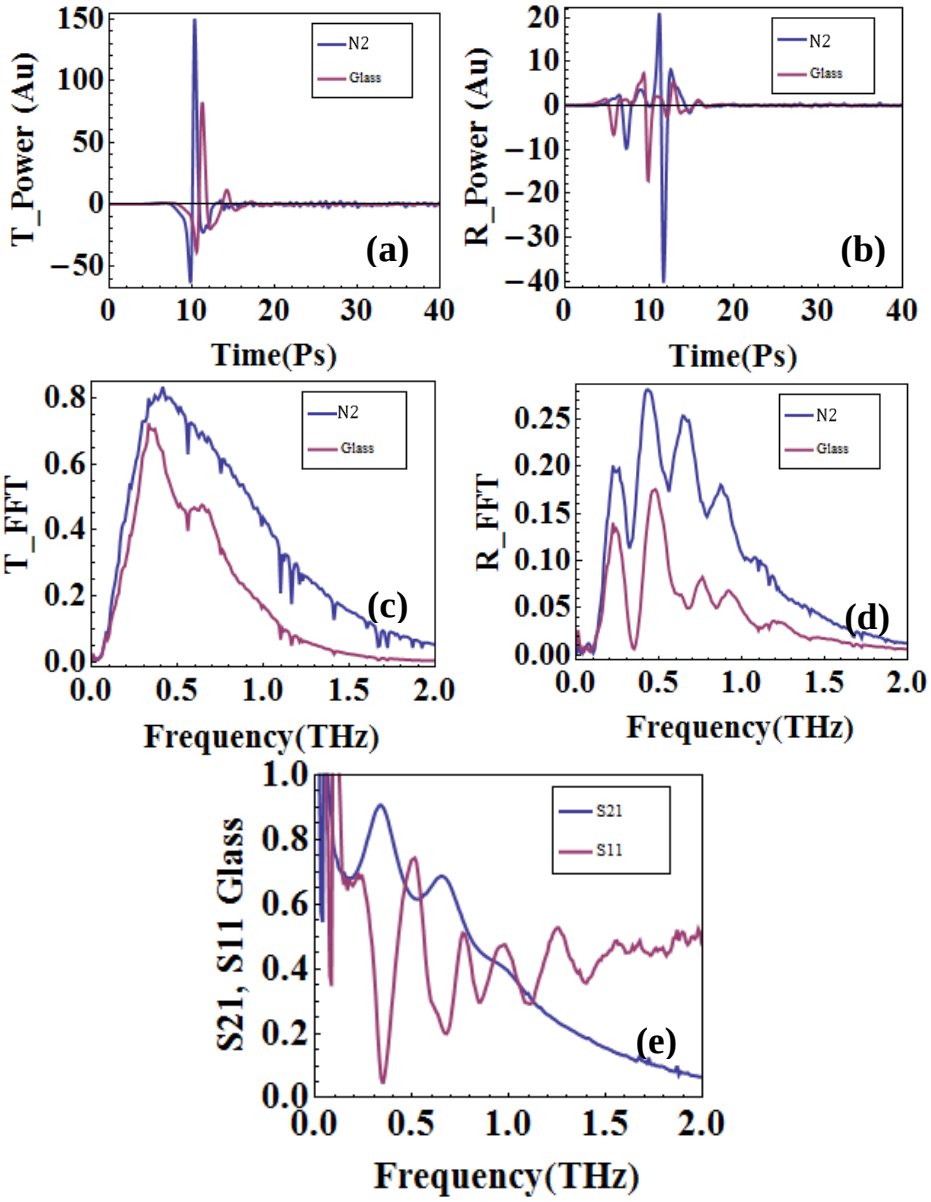

Figure 26: Transmission and reflection of VWR cover glass(180µm) measurements (a-b) transmission and reflection in time domain and nitrogen reference, (c-d) converting transmission and reflection by FFT to frequency domain, (e) normalize

transmission and reflection of glass to nitrogen in frequency domain and obtain S21 and S11

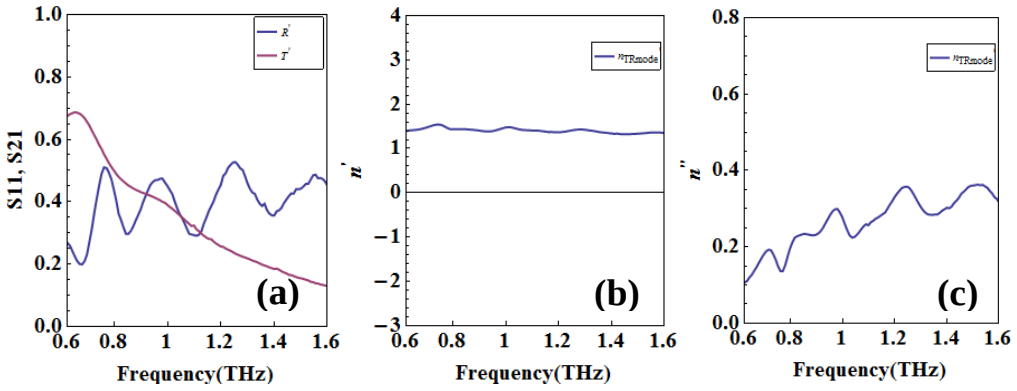

Figure 27: Complex refractive index of VWR cover glass (180 µm) calculated from transmission and reflections with Fabry-Perot effect. (a) Real part of S21 and S11 from 0.6 to 1.6 THz, (b-c) real and imaginary part of refractive index (n' and n'')

4.1.3 Transmissions of different substrates

Our metamaterial design (10um) requires a supporting substrate. Thus, the material properties of the substrate become important. If the substrate is highly absorptive of THz radiation, characterization of metamaterial from transmission becomes difficult. We investigated the transmission of four different substrates; (1) cover glass (VWR, USA), (2) Durimide 7520 polyimide film (Fuji film, Japan), (3) PTFE film (USA) and (4) High resistance (resistivity > 10000 ohm/cm, China) silicon wafer. Transmission of polyimide (Durimide 7520) and PTFE film are between 0.8 and 1 (Figure 28b-c). Polyimide and PTFE film are soft and easily bent, and therefore not good choices for substrates. Thus, rigid VWR cover glass and silicon wafer are good candidates. The transmission of VWR glass decreases significantly from 0.6~1.6THz. However, the averaged transmission of 1mm silicon remains almost constant from 0 to 3 THz except for significant Fabry-Perot effects. As mentioned in 4.1.2, Fabry-Perot effect of 1 mm silicon can be removed by the time-window technique. The time domain signal of 1mm silicon referenced to nitrogen (Figure 29a) shows that 4 transmission modes can be clearly separated. After applying a time-window to remove signals after 38ps and transforming the time domain signal to

frequency domain by FFT, we can see the Fabry-Perot effect is removed (Figure 29b). Hence, to avoid weak transmission signal and the Fabry-Perot effect from substrate, we chose the 1mm thick silicon as substrate. The comparison of transmission of different substrates is shown in Table 3.

VWR cover Glass (180μm)	Durimide 7520 (15μm)	PTFE film (381μm)	High resistive silicon (1mm)
Pros: ● Optically and UV transparent ● good for micro fabrication: back side exposure and alignment Cons: ● Lossy above 0.7 THz	Pros: ● Good transmission 0.8~1(0~1.5THz) Cons: ● Soft and makes fabrication difficult	Pros: ● High transmission 0.9~1 (0~1.5THz) Cons: ● Soft and makes fabrication difficult	Pros: ● Good transmission 0.6~1 (0~1.5THz) ● good for micro fabrication

Table 3: Comparison of transmission of different substrates

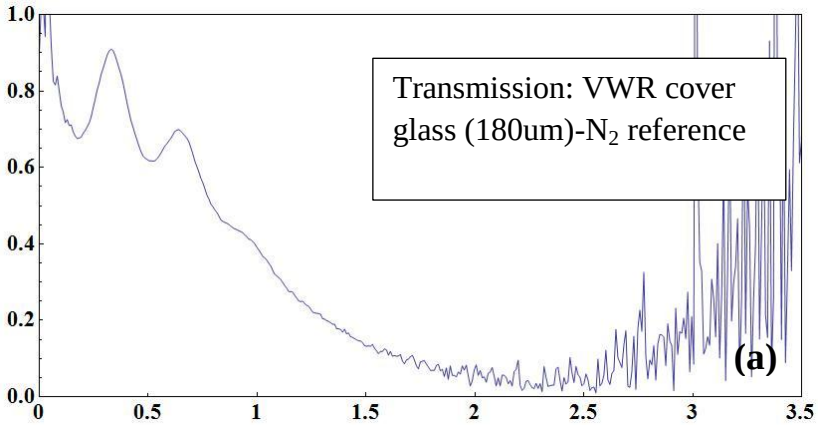

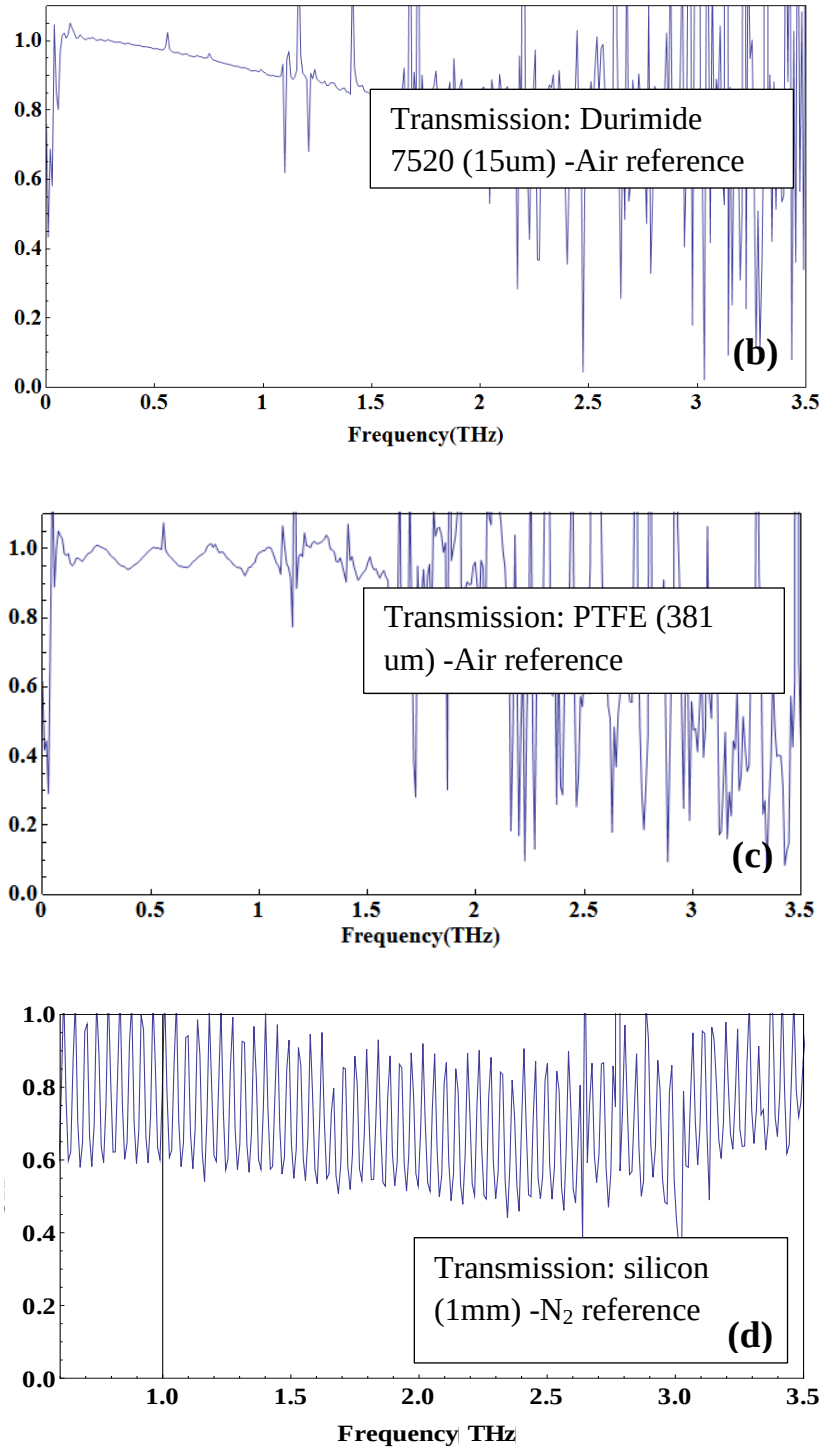

Figure 28: Transmission of (a) cover glass, (b) polyimide film, (c) PTFE film and (d) silicon

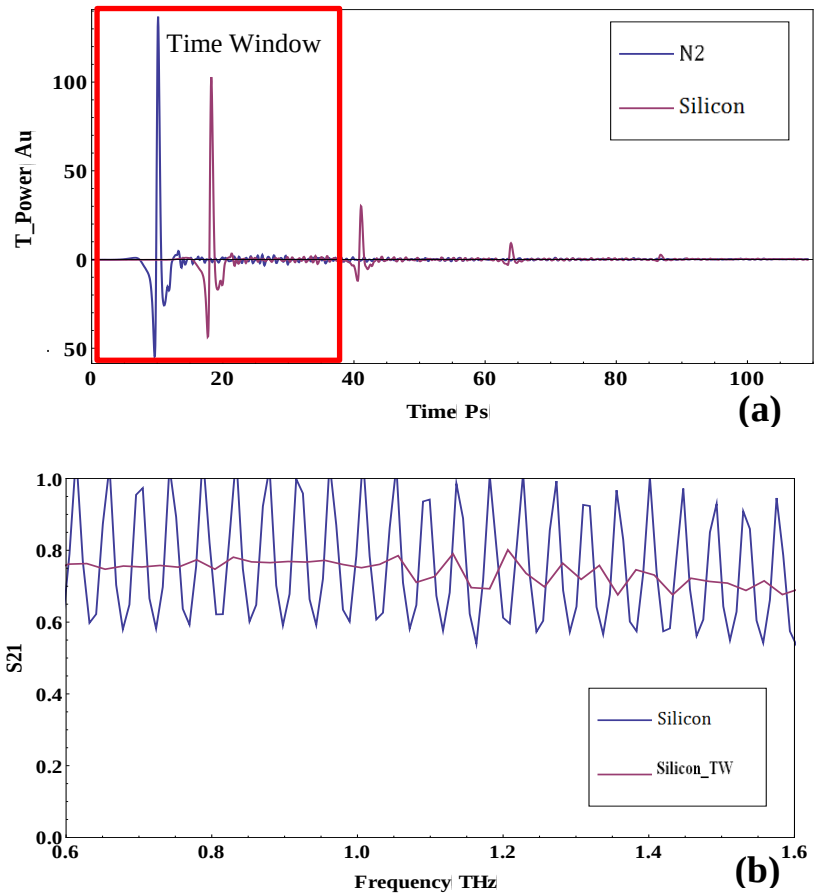

Figure 29: (a) time domain signal of silicon (1mm) with nitrogen reference. 4 reflection modes can be clearly separated in time domain (b) transmission of silicon (1mm) referenced to nitrogen. The Fabry-Perot effect of the original signal can be removed by applying the time-window technique

4.2 Characterization of non-tunable SU8 fishnet metamaterial

A non-tunable SU8 fishnet metamaterial is first fabricated and characterized to validate the model developed in chapter 3 because the material properties of SU8 is well-studied [56]. A fishnet metamaterial infiltrated with SU8 photoresist (fully cured) is fabricated on 1 mm silicon substrate with 10nm Titanium as an adhesion layer (Figure 30). The thickness of both top and bottom electrodes are 250nm. The thickness of SU8 is 4.75μm. The dimensions of the fishnet metamaterial are shown in Figure 31b. B is the net part of the fishnet pattern (6μm) which is originally designed to be 10μm. A is the

dimension of the square (112µm) which is originally designed to be 115µm. The reduced dimensions arise from fabrication errors during gold etching. The testing sample (Figure 31a) is divided into three areas: silicon, fishnet and the bottom gold layer. The silicon area is where the reference signal of the substrate is measured. The signal of the sample is measured at the fishnet area. In the transmission mode of THz-TDS, the electric field of sample is normalized to the reference measurement to obtain transmission (Figure 32a). In the reflection mode (Figure 32b), the reference signal is obtained by reflecting THz field from a silver lens. The surface of the silver lens is placed at the same plane as fishnet sample to avoid phase differences between sample and reference.

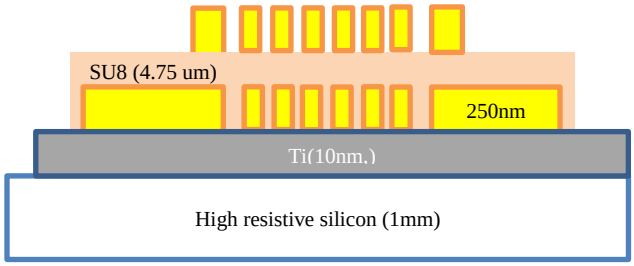

Figure 30: SU8 fishnet metamaterial on 1 mm silicon substrate

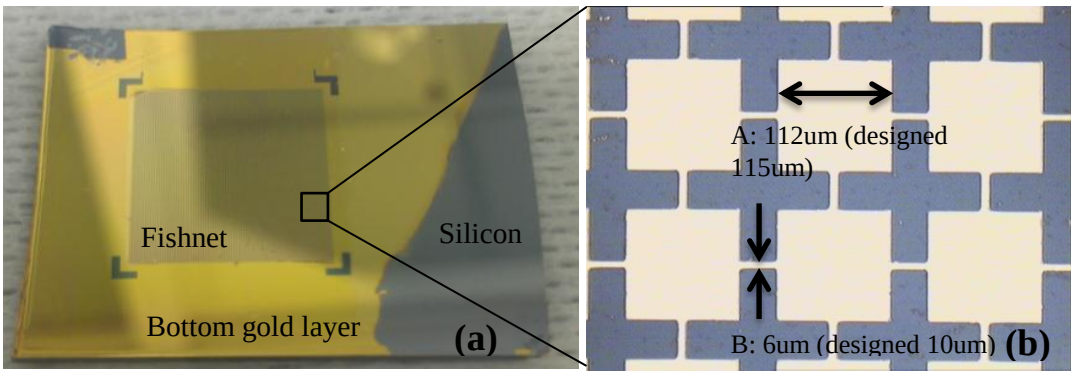

Figure 31: SU8 fishnet metamaterial, (a) testing sample (b) dimensions of fishnet metamaterial after fabrication

The transmission and reflection of SU8 fishnet metamaterial without Fabry-Perot effect are shown in Figure 32c-d. Compared to simulation results, the transmission dip (0.6THz) of the experiment results shift 0.2 THz to the left. This resonant frequency shift could be a result of misalignment of top and bottom electrodes or by the dielectric constant of SU8 is being different from the constant (1.79) used in the simulation. Furthermore, there are two resonant dips of reflection in the simulation results. One occurs at 0.95THz, is due to fishnet pattern itself. The resonance of fishnet pattern is similar to a frequency selective surface (FSS) and is induced mainly by the electric field. Thus, it is called electric resonance. The other resonant dip occurs at 0.8 THz and is caused by the inductance from top and bottom of the fishnet pattern. This resonance is called magnetic resonance because the inductor-like fishnet metamaterial couples the magnetic field into resonant current. However, the reflection dip of magnetic resonance is not clear in the experiment result. This might be due to the resolution of THz-TDS system is not enough. The duration of the probing pulse (0.05 to 0.15 ps) sets the resolution in time domain: this can be seen from the missing peaks of Fabry-Perot effect of 1mm silicon (Figure 29b). Another possible reason might be that the electric resonance and magnetic resonance are merged into one resonant dip due to fabrication error and cannot be clearly distinguished. Compared to the simulation results, the major reflection dips in the experimental results (0.8 THz) shift 0.15 THz to the left.

The refractive index of SU8 fishnet metamaterial is calculated by eq. 6, with the transmission and reflection coefficient obtained from experiment. Compared to simulation results, the dip of real refractive index (Figure 33a) shift 0.2 THz to the left with a minimum value of -13. The imaginary refractive index (Figure 33b) is positive which satisfy the criteria in eq. 8. The pattern of the imaginary refractive index also matches with the simulation result, except for the frequency shift.

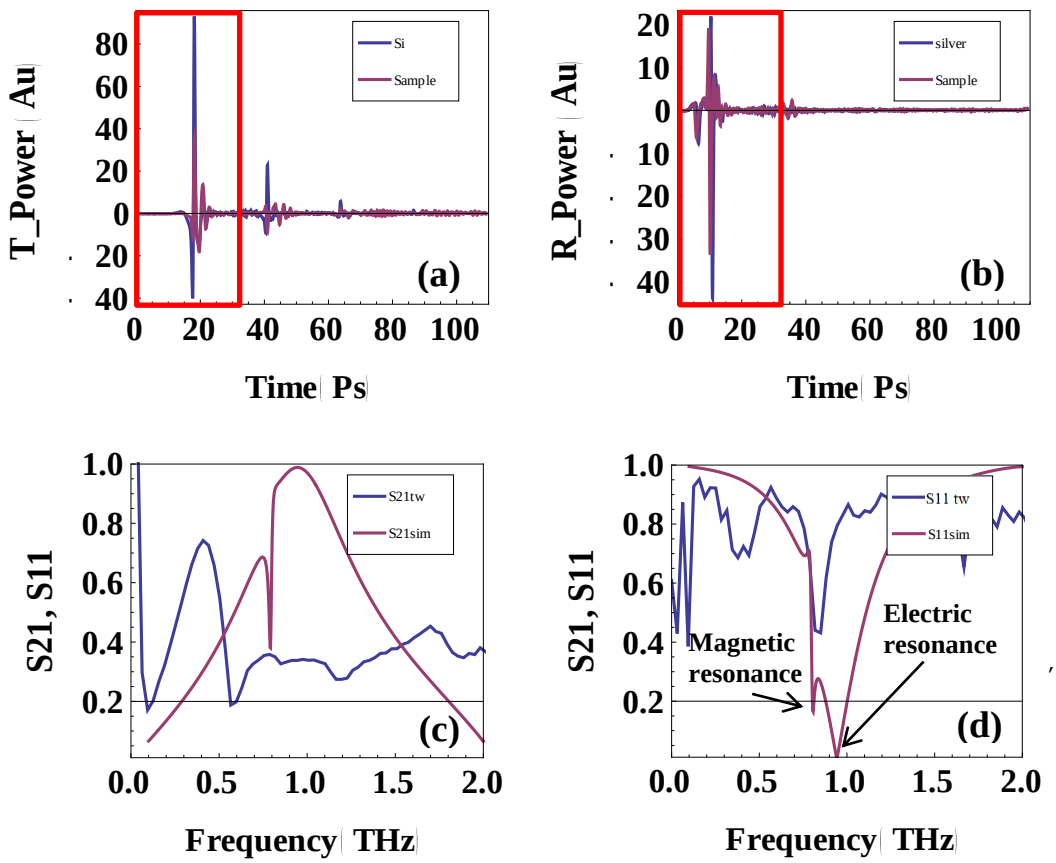

Figure 32: Characterization of SU8 fishnet metamaterial by THz-TDS, (a) electric field of fishnet sample (purple) and substrate (blue) in transmission mode. The time window (red) is applied to remove Fabry-Perot effect (b) electric field of fishnet sample (purple) and silver lens (blue) in reflection mode, The same time window (red) as used in transmission mode is also applied (c) transmission (S21) of SU8 fishnet metamaterial (blue) and simulation result (purple) (d) reflection (S11) of SU8 fishnet metamaterial (blue) and simulation result (purple). Two resonance dips can be clearly seen in simulation result but only one resonant dip is found in experiment result

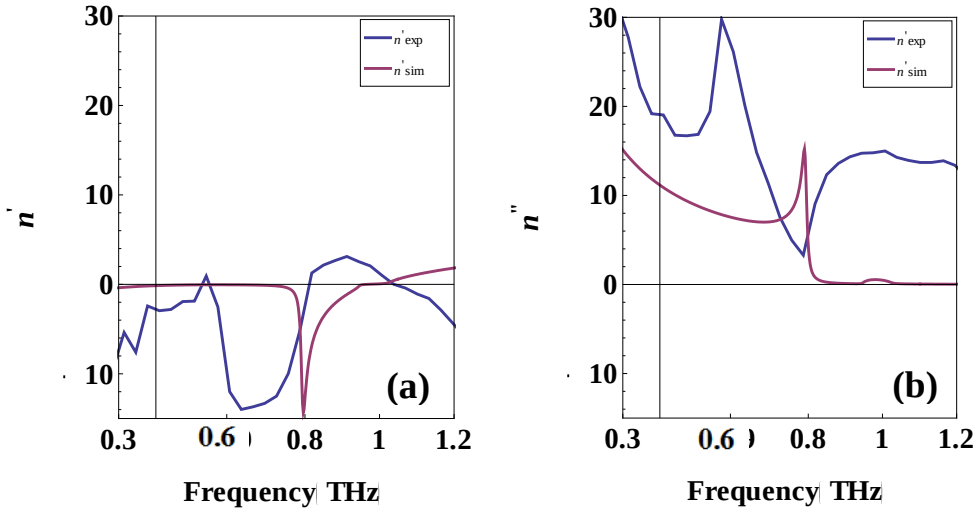

Figure 33: Refractive index of SU8 fishnet metamaterial

4.3 Introduction to PDLC and encapsulation technique

The PDLC used in TFMM is a two-phase material consisting of host polymer and liquid crystal. The liquid crystal is 4-pentyl-4'-cyano-biphenyl (5BC) and host is an inactive acrylate based polymer. The amount of 5CB in pre-polymer solution is 45 wt%. The remaining parts of the solution are acrylate pre-polymer and primer. During the photo curing process, pre-polymer will be polymerized while 5CB will be encapsulated and form liquid crystal droplets. When PDLC is in the off-state, with no electrical field applied (Figure 34a), the liquid crystal molecules are anchored by the polymer matrix in a random configuration. The refracted index differences between polymer matrix and liquid crystal creates scattering when light transmitted through the PDLC. In this state, the PDLC is opaque. However, if an external electrical field is applied, the liquid crystal molecules are aligned to the field and light can be transmitted (Figure 34b). In this state, PDLC is transparent. When the electrical field is removed, the anchoring force of the polymer matrix pulls the liquid crystal molecules back to random configuration. Hence, the PDLC once again become opaque.

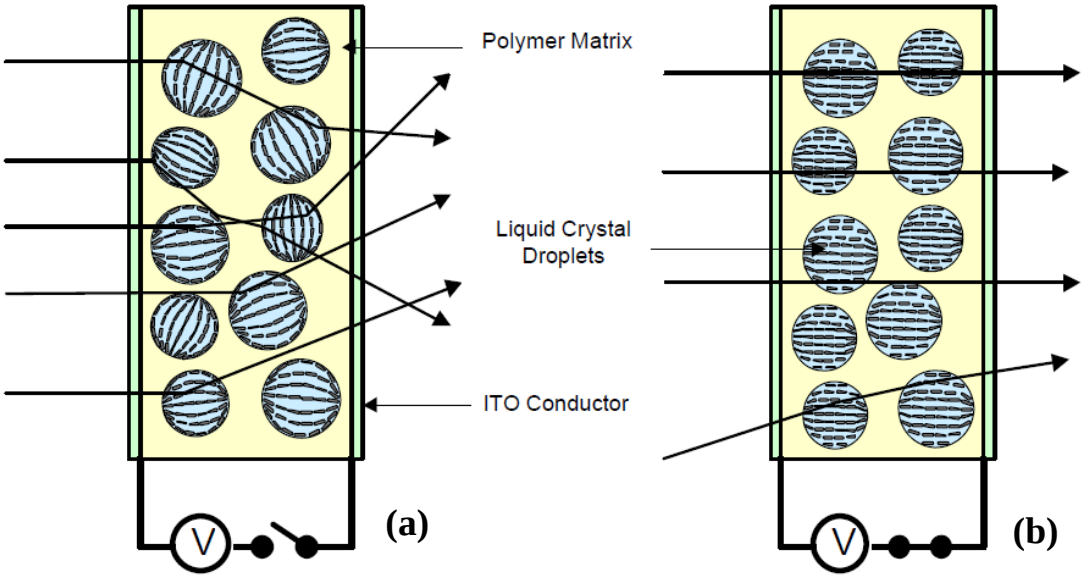

Figure 34: (a) PDLC film in the off-state; no external electrical field is applied. Liquid crystal encapsulated by polymer matrix is in random configuration. (b) PDLC film in the on-state; the liquid crystal molecules are aligned with the external electrical field. When the external electrical is removed, the liquid crystal molecules return to a random configuration due to the anchoring force provided by polymer matrix.

The major challenge of fabricating a PDLC-TFMM lies in how to deposit metal layer on PDLC. For a fishnet metamaterial infiltrated with inactive dielectric materials such as magnesium fluoride [23], metal deposition on dielectric is convenient because fishnet structures can be deposited in layers by E-beam evaporation or sputtering. However, these deposition methods are too energetic to safely deposit metal layer on PDLC without burning or otherwise damaging the structure of PDLC. Another issue of using PDLC as tunable dielectric material is that liquid crystal molecules inside PDLC tend to escape from polymer matrix and form liquid crystal droplets on the surface of PDLC film. This will increase the surface roughness and chance of shorting the top and bottom fishnet electrodes. Thus, in order to maintain the functionality of PDLC and prevent shorting issue during metal deposition process, a novel technique that utilizes a thin polyimide layer (skin layer) to protect the PDLC is applied.

A PDLC (6μm) film covered by polyimide (1.5μm) skin layer with only top gold fishnet pattern is fabricated (Figure 35a) to prove that polyimide skin layer can successfully cover the PDLC and enable metal deposition. The entire sample is made on Indium Tin Oxide (ITO) glass and the electric field can be applied between ITO and fishnet electrode to show the optical tuning effect. As shown in Figure 35c, the gold, behind the transparent PDLC reflects the image of an object (a camera with two LED lights) at a 260V bias. A microscopic view of the sample (Figure 35e) shows that fringe effect of the electric field can turn PDLC cloudy around the fishnet electrode. Thus, the appearance of cloudy PDLC around the fishnet electrode shows that the PDLC is turned on. This observation is especially useful to tell the on and off state of a PDLC-TFMM when it is made on optically opaque substrates.

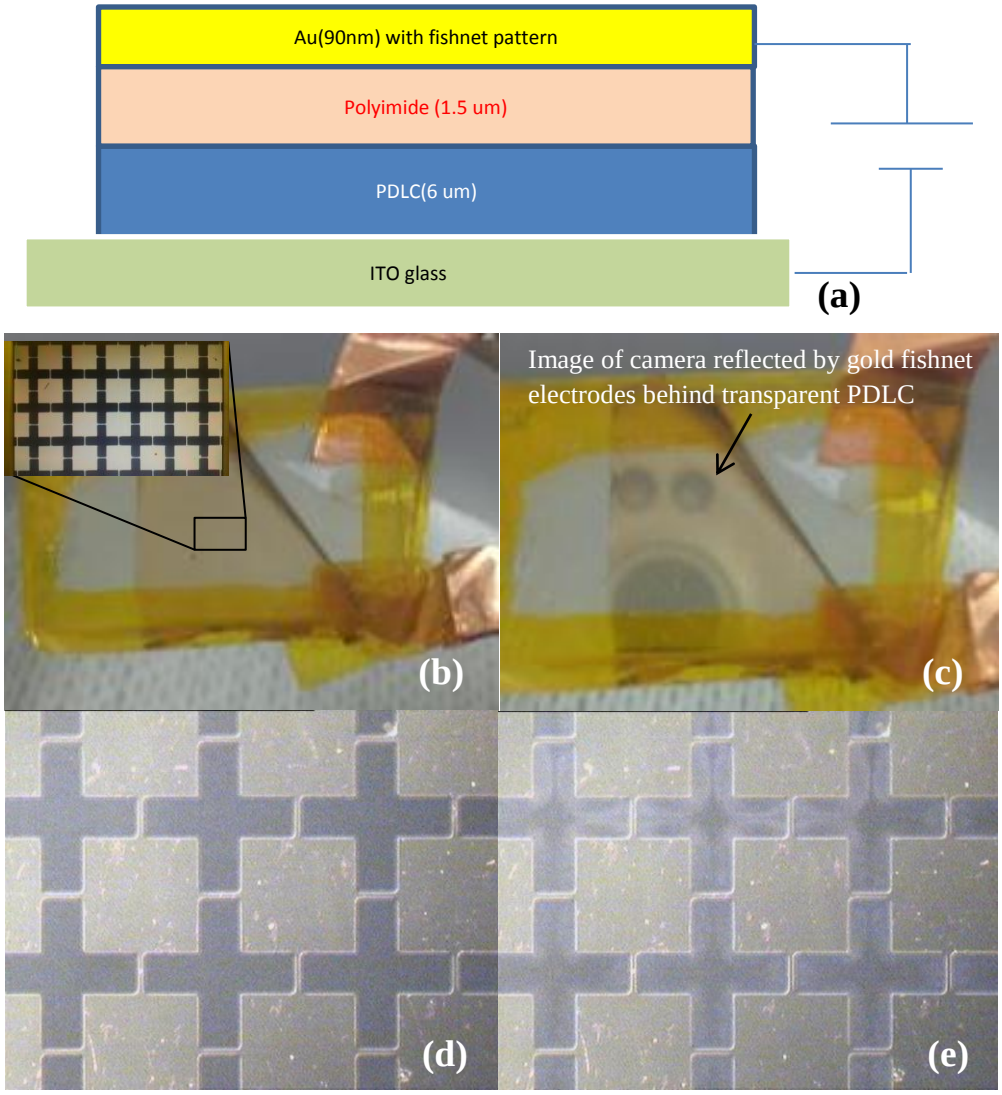

Figure 35: Tuning effect of PDLC with fishnet and ITO electrodes (a) gold fishnet pattern is fabricated on polyimide/PDLC/ITO composite (b) overhead view of device from bottom side (ITO) of the sample with no bias (c) overhead view of the sample at 260V bias (d) microscopic view of sample with no bias (d) microscopic view of sample at 260V bias

4.4 Characterization of tunable PDLC fishnet metamaterial

Similar to SU8 fishnet metamaterial introduced in section 4.2, the PDLC-TFMM is also fabricated on 1mm silicon substrate (Figure 36). The PDLC (10μm) is covered with the polyimide (1.5μm) skin layer. The thickness of top and bottom gold electrodes

(fishnet) are both 250nm. The adhesion layer between gold and silicon is the chromium (5nm).The chromium is patterned by using the gold fishnet as hard mask. The bias voltage is provided direct from top and bottom fishnet electrodes.

Two measuring areas are fabricated on the sample (Figure 37a); fishnet metamaterial and silicon substrate without chromium adhesion layer. The top and bottom fishnet electrodes are separated by PDCL layer and the copper tape is used as wires to connect top and bottom electrodes to power supply. So far, there is no other direct method that can help us observing the condition of PDLC under the fishnet electrodes. Hence, we use the fringe effect of the electric field to help us decide the on and off state of PDLC. As shown in Figure 37c, there is a significant fringe effect of the electric field around fishnet electrode at 280V bias. The originally dark PDLC around fishnet electrode (Figure 37b) becomes cloudy and bright after 280V bias is applied. When PDLC becomes cloudy and fringe effect is strong, the PDLC is on. If the voltage applied is larger than 280V, the dielectric breakdown occurs easily around the net part of the fishnet (Figure 38). The possible reason for dielectric breakdown may come from the charge accumulation around sharp edges of the fishnet electrode.

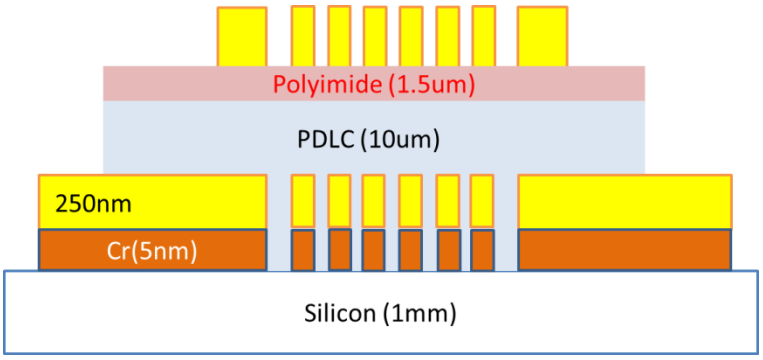

Figure 36: Tunable fishnet metamaterial infiltrated with PDLC (PDLC-TFMM)

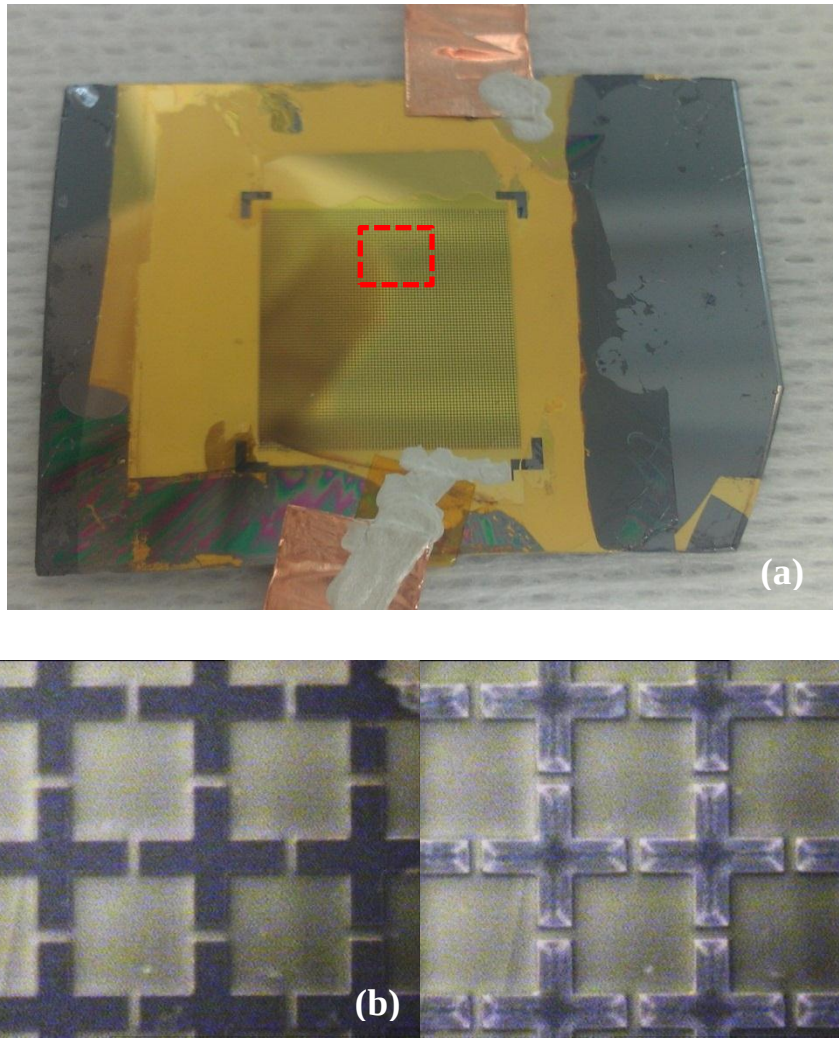

Figure 37, Tunable PDLC fishnet metamaterial, (a) overhead view of the sample (b) zoomed view (red and dashed square in (a)) of PDLC fishnet metamaterial at 0V bias (c) 280V bias applied to PDLC fishnet metamaterial. Fringe effect of electrical field around the fishnet electrode turns the PDLC on.

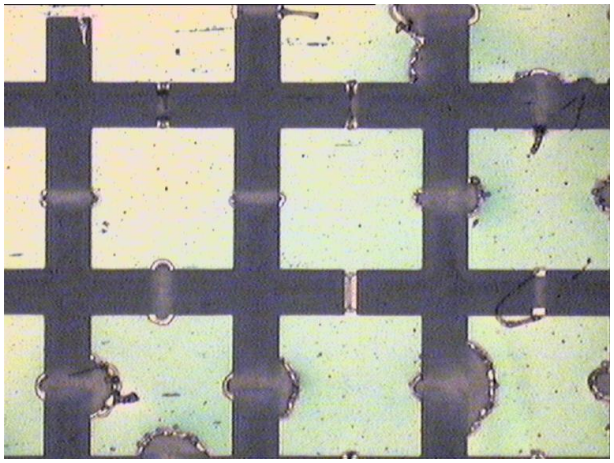

Figure 38: Dielectric breakdown of PDLC fishnet metamaterial at net part

The transmission and the reflection of PDLC metamaterial at 0V bias are shown in Figure 39a. Transmission is obtained by normalizing the electric field of fishnet area to the electric field of 1mm silicon substrate. Reflection is obtained by normalizing the electric field of fishnet area to that of silver lens. Similar to the transmission and the refection of SU8 fishnet metamaterial, the transmission dip of PDLC occurs at 0.6THz and the reflection dip occurs at 0.88 THz. The phase jumps of transmission and the reflection also occur around these frequencies (Figure 39b). The real refractive index dip occurs at 0.55THz with a value of -13 (Figure 40). The imaginary refractive index is all positive, which satisfies the criteria in eq.8

The reflection of the PDLC fishnet metamaterial is measured at 0V and 280V bias. The resonant dip shifts from 0.87 to 0.86 THz giving a total frequency shift of 0.01 THz (Figure 41a). Compared to the simulation results of fishnet metamaterial infiltrated with 100% liquid crystal, where the resonant dip shifts 0.06 THz (Figure 15b), the range of the resonant dip shift of PDLC fishnet metamaterial drops 83%. It is clear that the diluted liquid crystal (45 wt %) inside PDLC polymer matrix contributes to the drop of shifting range because the overall dielectric constant change of PDLC is less than that of pure liquid crystal.

Another possible cause for the drop of shifting range is due to the alignment of liquid crystal inside PDLC. Without a proper alignment layer, liquid crystal molecules in PDLC are in a random configuration in the off state (Figure 34a). However, in the simulation,

the dielectric constant change of liquid crystal is ideal, with perfectly orthogonal alignments of liquid crystal molecules between the on and off states.

The transmission coefficients of PDLC sample at 0V and 280V are also investigated. However, the tunable range of PDLC metamaterial drops over time, preventing consistent measurements of dielectric constant change. Thus, significant frequency shifts of transmission cannot be observed. It is possible that the liquid crystal is over driven by the electric field, fixing the molecules in the 'on' state even when the field is removed.

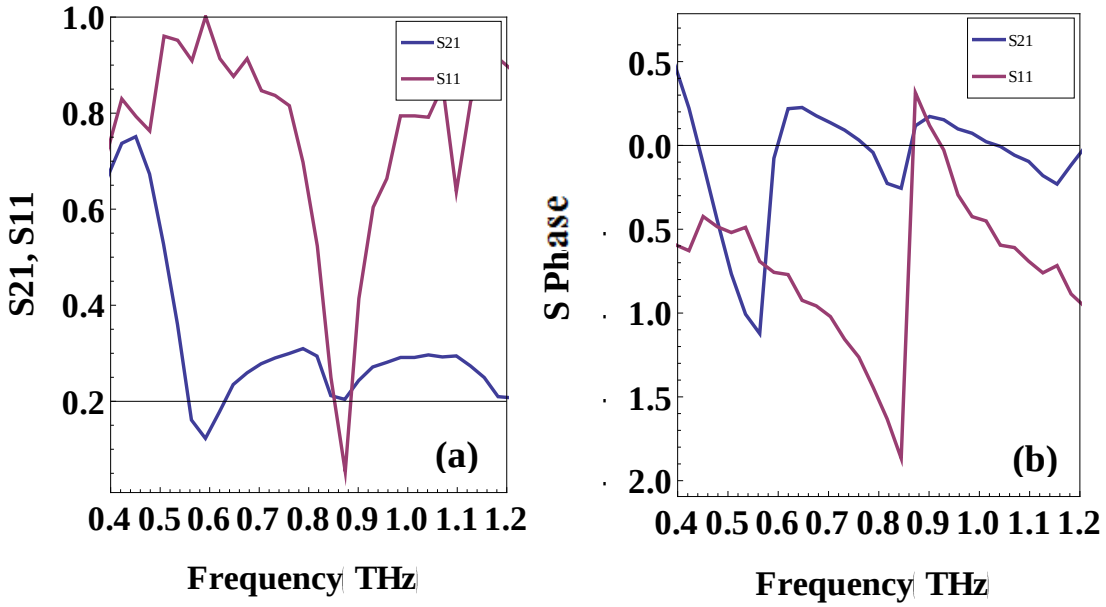

Figure 39: Transmission and reflection of PDLC fishnet metamaterial at 0V bias, (a) magnitude of transmission (S21) and reflection (S11) (b) phase of transmission (S21) and reflection (S11)

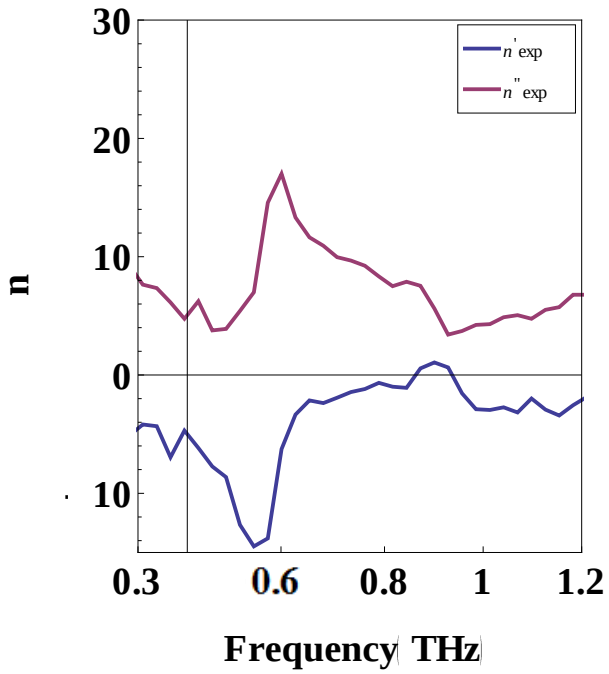

Figure 40: Refractive index of PDLC fishnet metamaterial at 0V bias

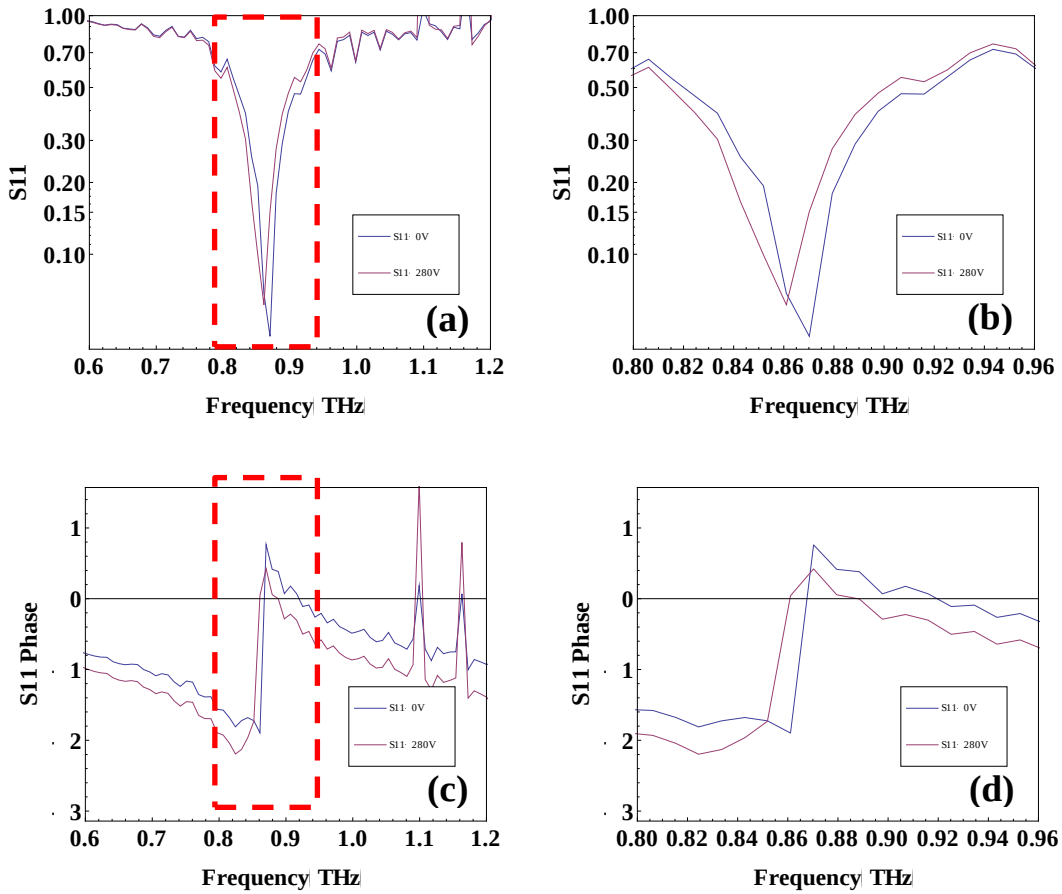

Figure 41: Reflection of PDLC fishnet metamaterial at 0V and 280V bias, (a-b) magnitude of reflection and zoomed view (red-dashed square) (c-b) phase of reflection and zoomed view (red-dashed square)

Chapter 5

Conclusion and future considerations

5.1 Conclusion

The motivation of our work was highlighted in the beginning of the first chapter. The large refractive index change in the tunable fishnet metamaterial (TFMM) shows its potential as a wide-angle beam steering device. The second chapter shows the basic design of a fishnet metamaterial can be modeled based on a simple RLC circuit. The chapter also describes that a fishnet metamaterial design is simply a 3D rendition of a planar split ring resonator.

Chapter three contains technique and theory which describe the derivation of constitutive parameters of a single layer fishnet metamaterial (SLFM) from transmission and reflection. Our study of SLFM shows that a negative ε'' is an intrinsic property of SLFM. It also suggests that the selection of arccosine branches should come from the off-resonant band to avoid the anti-resonant phenomenon. This phenomenon causes the sign of the imaginary permittivity ε'' to be opposite that of the imaginary permeability μ" . We also reported that the negative refractive index of SLFM near the resonant band does not cause the wavelength to be smaller than unit cell size in the direction of wave propagation. This validates the effective medium assumption. The study of $|n'|$ by adding different thickness of PI in the SLFM structure confirms that wavelengths near the resonant frequency are still larger than the unit cell size. However, the resulting effective index might not be truly representative of the index of SLFM. Lastly, we show that by increase the unit cell size in the propagating direction, one can reduce the effects of the anti-resonant phenomenon but cannot retain the negative refractive index value.

Also in chapter three, we numerically demonstrated the tunability of SLFM and multilayer fishnet metamaterial (MLFM) in THz range using the liquid crystal. The design takes actual fabrication into consideration by using flexible polyimide as substrate to hold and seal the liquid crystals. We also demonstrated a robust means of finding the reference plane to retrieve the refractive index for multilayer fishnet metamaterial and

shown that resonance shift of the tunable metamaterial can be explained by a RLC circuit model. However, more study is required to find the causes of the discontinued refractive index in MLFM

Chapter four describes the fabrication and measurement of our tunable PDLC and non-tunable SU8 fishnet metamaterials. THz-TDS is used to obtained the transmission and reflection coefficients for the devices. In the fabrication, we show that a skin layer made of polyimide is necessary to prevent the escape of liquid crystal from the polymer matrix and enable a smooth metal electrode deposition. Furthermore, transmissions of different substrates are measured and 1 mm thick silicon substrate is chosen.

Also, in chapter four, the concept of tuning the resonant frequency of fishnet metamaterial is proven by changes in its dielectric constant. The tuning frequency range is 0.01 THz and it is 83% less than the tuning range in the simulation (0.06THz). The discrepancy in tuning range can be explained by the lower content of liquid crystal in PDLC and the misalignment of the incident beam and the optical axis of liquid crystal molecules. The negative refractive index of designed fishnet metamaterial is shown to be -13 for both SU8 and PDLC fishnet metamaterials.

Finally, the device was tested at its operating limit. We found that the dielectric breakdown mainly occurs around the corners of the fishnet electrode, suggesting charge accumulation in those areas. We also notice there is gradual degradation of the PDLC refractive index change over time. One possible explanation is that PDLC is driven over its threshold field limit, causing some liquid crystal molecules inside polymer matrix to be permanently affixed in the direction of the applied electric field.

5.2 Future considerations

5.2.1 Improvements

There are several immediate improvements that can be implemented to the current design. Rounding the corners of the fishnet electrode, as shown in Figure 42, may prevent the dielectric breakdown observed in the current design.

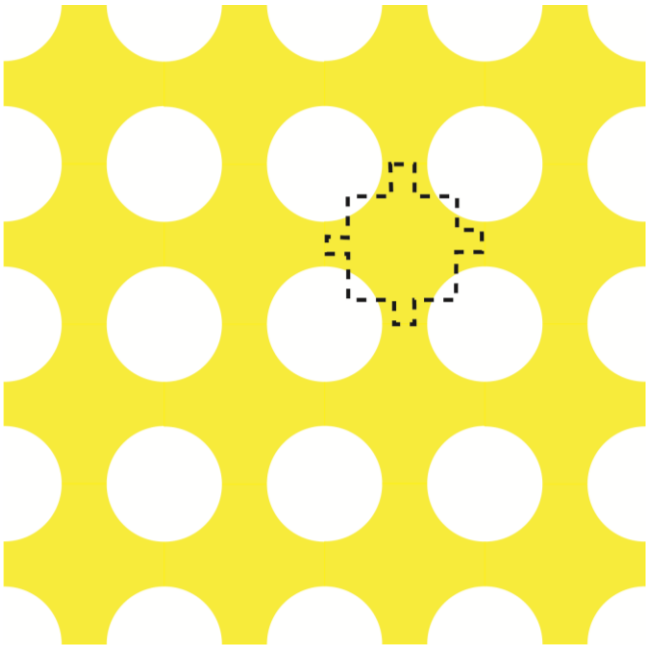

Figure 42: An improved fishnet metamaterial design, rounding the sharp edges of the previous pattern. The dashed line is the current fishnet unit cell design and the yellow area is the new design with its unit cells arranged periodically.

Second, the tuning range of current PDLC fishnet metamaterial is much less than the result from simulation. This could be due to the random orientation of the liquid crystal molecules inside the unbiased polymer matrix. If the liquid crystal molecules inside the PDLC matrix can be pre-aligned 90 degrees from the field direction, the effective index change could be greatly improved. The pre-alignment of liquid crystals can be achieved by creating an alignment layer similar to the regular alignment layer for liquid crystal [57] (Figure 43).

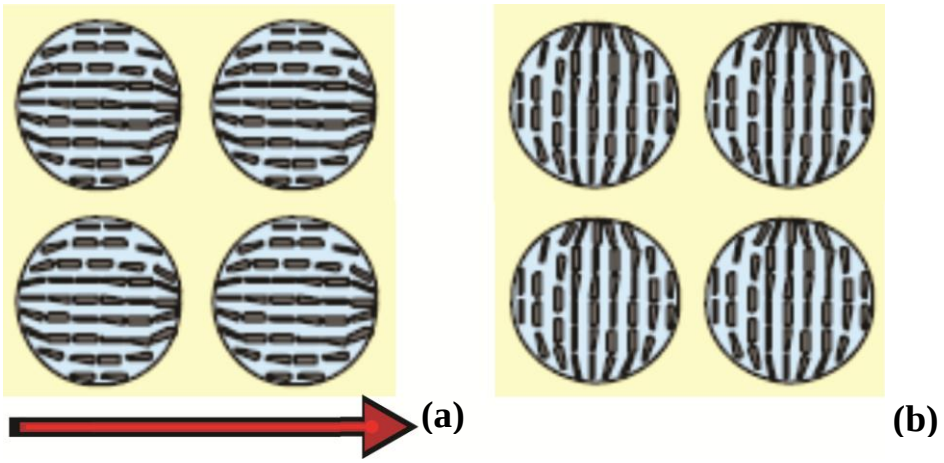

Figure 43: (a) aligned PDLC in off state, red arrow show the direction of alignment layer (b) PDLC aligned by external electric field at on state

5.2.2 Beam deflecting prism design

The idea of designing a TFMM prism for beam steering purpose is similar to a regular prism design, except that the fishnet is an anisotropic material which only allows normal beam incident (Figure 44). Therefore, the stacked fishnet prism design is utilized to create the large optical path difference (OPD) needed to achieve large angle beam steering. The optical path length (OPL) of the incident electromagnetic wave can be formulated as follows:

$$OPL = \int_{d1}^{d2} n(s)ds \quad \text{.....(21)}$$

where *s* is the path of EM wave, *n(s)* is the refractive index as a function of *s*, and (*d1-d2)* is the thickness of the material. If the material is homogeneous, than the OPD can be written as

$$OPD = n\,(d1 - d2) \ldots\ldots (22)$$

The concept of using OPD to create beam steering device is not difficult. However, finding a material with a large refractive index change to steer the beam is not easy. For example, the ordinary and extra ordinary states of 5CB liquid crystal can shift the refractive index from 1.55 to 1.65, resulting in a 13.3% OPD change when the thickness is constant. Based on our preliminary results (Table 2), the proposed TFMM infiltrated with liquid crystal can shift the refractive index from -3 to -0.5 resulting in 83% OPD if operated at 1 THz.

To design a prism beam steering device for future work, two concepts can be applied: (i) a physical prism structure with multiple TFMM layers, (ii) a flat TFMM prism with gradient external fields. These design concepts are described in the following sections.

5.2.2.1 Physical TFMM prism design

To design a physical TFMM prism, we need to consider the geometry of single unit cell of TFMM, because it determines the aspect ratio of the fishnet prism structure. The number of unit cell has to be large enough so that the prism can be considered as a periodic structure. For example, the equivalent angle of a TFMM prism is determined by the ratio between *w* and *h*, as shown in Figure 44. The equivalent angle of the TFMM prism based the designed unit cell (*w* is 150 µm and *h* is 9.8 µm) is 11.09 degrees when polyimide layer is removed (Figure 8c). Based on Snell's law, when the wave is incident normal on the TFMM prism, the output angle θ_1 can be calculated by

$$\theta_1 = \sin^{-1}\left(\frac{n_2}{n_1}\sin\theta_2\right) \ldots\ldots (23)$$

If the refractive index change is the same as the result from Table 2 at 1 THz, the output $\boldsymbol{\theta_1}$ can be tuned from -35.2 to -5.5 resulting in -29.7 degrees of tuning angle. The above case is considered when incident angle to the inclined surface of the prism is 11.09 degrees. There are two methods to increase the tuning angle: (i) increase the OPD between unit cell and its adjacent unit cell along the x direction, as shown in Figure 44. However, increasing the aspect ratio will also increase the total number of TFMM layers required and fabrication difficulty. (ii) Increase the resonant strength of TFMM so that changes of the refractive index can be increased. Figure 45 shows the physical TFMM prisms with high and low aspect ratios.

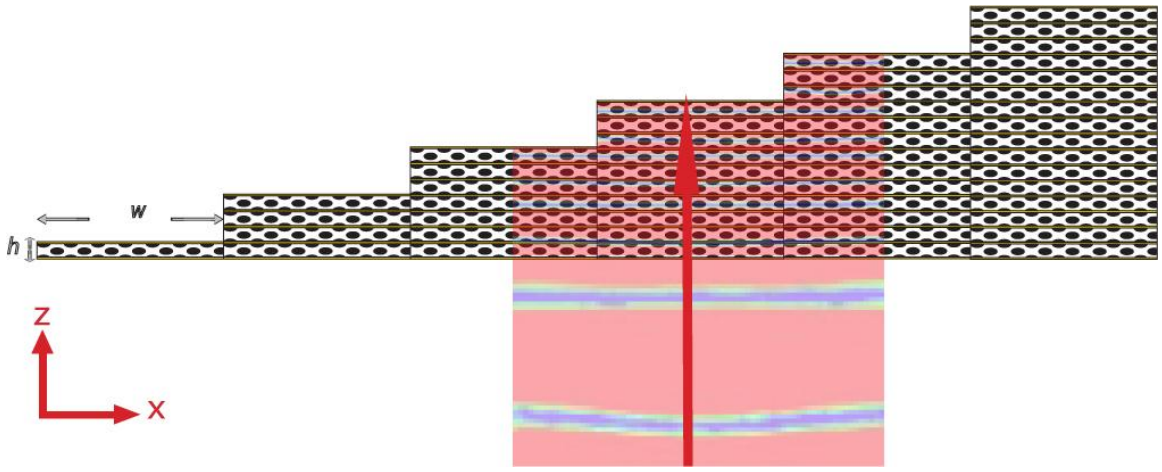

Figure 44: TFMM prism design, where the width *w* and height *h* of TFMM unit cell are 150 µm and 9.8 µm, respectively. The incident wave travelling in z direction and each three-layer increment of TFMM along the x direction creates 11.09 degree prism design.

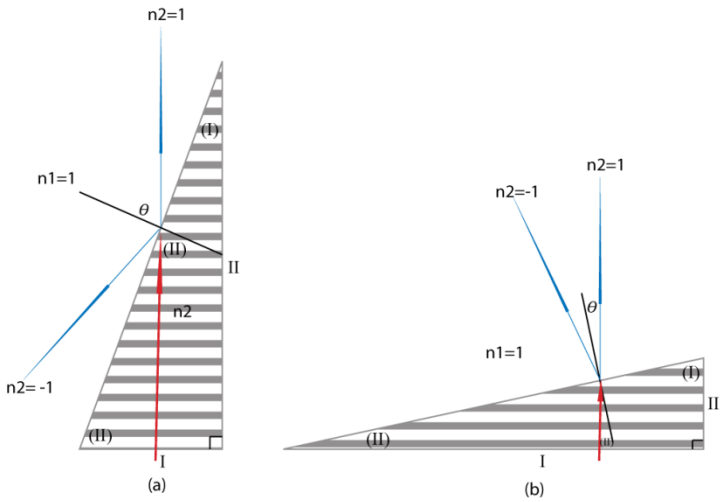

Figure 45: Multilayer TFMM with different aspect ratios: (a) high aspect ratio could result in a large tuning angle. However, more layers of fishnet metamaterial are required, increasing the difficulty of fabrication (b) A low aspect ratio fishnet structure can alleviate fabrication challenge, at the cost of decreasing the maximum tuning angle

5.2.2.2 Flat TFMM prism design

The fabrication challenge of making multilayer TFMM prism can be alleviated with a flat prism structure by combining (i) the concept of beam steering based on OPD and (ii) the large refractive index change of metamaterial near its resonant frequency. To steer the beam by prism, it is not necessary to make the beam steering device a physical prism shape, as long as the material can create a large OPD varied along the direction perpendicular to incident EM wave. Since TFMM can create large refractive index changes, the fishnet structure can be used as individual electrode to apply separate electric field onto the PDLC, resulting in a gradient refractive index along the direction perpendicular to incident EM wave, equivalent to a real prism.

Bibliography

[1] X. C. Zhang, "Terahertz wave imaging: horizons and hurdles," *Physics in Medicine and Biology,* vol. 47, pp. 3667-3677, 2002.

[2] H. Quast and T. Loffler, "3D-terahertz-tomography for material inspection and security," in *Infrared, Millimeter, and Terahertz Waves, 2009. IRMMW-THz 2009. 34th International Conference on*, 2009, pp. 1-2.

[3] N. N. Kudryavtseva and et al., "Behavioral effect of terahertz waves in male mice," *Bulletin of Experimental Biology and Medicine,* 2008.

[4] S. Nathan and et al., "Dielectric properties of biological molecules in the Terahertz gap," *Applied Physics Letters,* vol. 87, p. 113901, 2005.

[5] B. S. Alexandrov, V. Gelev, A. R. Bishop, A. Usheva, and K. Ø. Rasmussen, "DNA breathing dynamics in the presence of a terahertz field," *Physics Letters A,* vol. 374, pp. 1214-1217, 2010.

[6] B. B. Hu and M. C. Nuss, "Imaging with terahertz waves," *Opt. Lett.,* vol. 20, pp. 1716-1718, 1995.

[7] A. J. Fitzgerald and et al., "An introduction to medical imaging with coherent terahertz frequency radiation," *Physics in Medicine and Biology,* vol. 47, p. R67, 2002.

[8] K. Kawase, Y. Ogawa, Y. Watanabe, and H. Inoue, "Non-destructive terahertz imaging of illicit drugs using spectral fingerprints," *Opt. Express,* vol. 11, pp. 2549-2554, 2003.

[9] H. L. Edmund and et al., "Terahertz Pulse Imaging of ex vivo Basal Cell Carcinoma," *Journal of Investigative Dermatology,* vol. 120, p. 72, 2003.

[10] R. M. Woodward, V. P. Wallace, D. D. Arnone, E. H. Linfield, and M. Pepper, "Terahertz Pulsed Imaging of Skin Cancer in the Time and Frequency Domain," *Journal of Biological Physics,* vol. 29, pp. 257-259, 2003.

[11] P. H. Siegel, "Terahertz Technology in Biology and Medicine," *IEEE Transactions on Microwave Theory and Techniques,* vol. 52, p. 2438, 2004.

[12] T. Loffler and et al., "Visualization and classification in biomedical terahertz pulsed imaging," *Physics in Medicine and Biology,* vol. 47, p. 3847, 2002.

[13] L. Ho, M. Pepper, and P. Taday, "Terahertz spectroscopy: Signatures and fingerprints," *Nat Photon,* vol. 2, pp. 541-543, 2008.

[14] S. W. Smye, J. M. Chamberlain, A. J. Fitzgerald, and E. Berry, "The interaction between Terahertz radiation and biological tissue," *Physics in Medicine and Biology,* vol. 46, p. R101~R112, 2001.

[15] M. Usami and et al., "Development of a THz spectroscopic imaging system," *Physics in Medicine and Biology,* vol. 47, p. 3749, 2002.

[16] W.-C. Wang, J. Luo, and A. K. Y. Jen, "Electro-optic polymer prism beam deflector," *Optical Engineering,* vol. 48, pp. 114601-6, 2009.

[17] W. Wang, S. Lee, A. Jen, P. Reinhall, and D. Nuckley, "Development of an Electro-Optic Scanner for Potential Endoscope Application," *Journal of Medical Devices,* vol. 3, pp. 027522-1, 2009.

[18] Y. Jiang, Z. Cao, G. Chen, X. Dou, and Y. Chen, "Low voltage electro-optic polymer light modulator using attenuated total internal reflection," *Optics & Laser Technology,* vol. 33, pp. 417-420, 2001.

[19] J. Valentine, S. Zhang, T. Zentgraf, E. Ulin-Avila, D. A. Genov, G. Bartal, and X. Zhang, "Three-dimensional optical metamaterial with a negative refractive index," *Nature,* vol. 455, pp. 376-379, 2008.

[20] P. Ding, E. J. Liang, W. Q. Hu, L. Zhang, Q. Zhou, and Q. Z. Xue, "Numerical simulations of terahertz double-negative metamaterial with isotropic-like fishnet structure," *Photonics and Nanostructures - Fundamentals and Applications,* vol. 7, pp. 92-100, 2009.

[21] D. M. Mittleman, M. Gupta, R. Neelamani, R. G. Baraniuk, J. V. Rudd, and M.Koch, "Recent advances in terahertz imaging," *Appl. Phys. B,* vol. 68, pp. 1085–1094, 1999.

[22] V. G. Veselago, "THE ELECTRODYNAMICS OF SUBSTANCES WITH SIMULTANEOUSLY NEGATIVE VALUES OF epsilon AND mu," *SOVIET PHYSICS USPEKHI,* vol. 92, pp. 517-526, 1967.

[23] J. B. Pendry, A. J. Holden, D. J. Robbins, and W. J. Stewart, "Magnetism from Conductors and Enhanced Nonlinear Phenomena," *IEEE TRANSACTIONS ON MICROWAVE THEORY AND TECHNIQUES,* vol. 47, 1999.

[24] D. R. Smith, W. J. Padilla, D. C. Vier, S. C. Nemat-Nasser, and S. Schultz, "Composite Medium with Simultaneously Negative Permeability and Permittivity," *Physical Review Letters,* vol. 84, p. 4184, 2000.

[25] H. Y. Chen, X. Y. Hou, and L. J. Deng, "A Novel Microwave Absorbing Structure Using FSS Metamaterial," in *Progress In Electromagnetics Research Symposium Proceedings*, Moscow, Russia, 2009, p. 1195.

[26] C. Caloz and T. Itob, *Transmission line Theory and Microwave Applications*: Wiley-Interscience, 2006.

[27] A. Ishimaru, S. Jaruwatanadilok, and Y. Kuga, "GENERALIZED SURFACE PLASMON RESONANCE SENSORS USING METAMATERIALS AND NEGATIVE INDEX MATERIALS," *Progress In Electromagnetics Research, PIER,* vol. 51, pp. 139–152, 2005.

[28] C. CALOZ, *ELECTROMAGNETIC METAMATERIALS:TRANSMISSION LINE THEORY AND MICROWAVE APPLICATIONS*.

[29] E. Shamonina and L. Solymar, "Diamagnetic properties of metamaterials: a magnetostatic analogy," *Eur. Phys. J. B,* vol. 41, pp. 307-312, 2004.

[30] Y. Yuan, C. Bingham, T. Tyler, S. Palit, T. H. Hand, W. J. Padilla, D. R. Smith, N. M. Jokerst, and S. A. Cummer, "Dual-band planar electric metamaterial in the terahertz regime," *Opt. Express,* vol. 16, pp. 9746-9752, 2008.

[31] A. J. Taylor and et al., "Electrically resonant terahertz metamaterials: Theoretical and experimental investigations," *Physical Review B,* vol. 75, p. 041102, 2007.

[32] K. J. Malloy and et al., "Midinfrared Resonant Magnetic Nanostructures Exhibiting a Negative Permeability," *Physical Review Letters,* vol. 94, p. 037402, 2005.

[33] H.-T. Chen, W. J. Padilla, J. M. O. Zide, A. C. Gossard, A. J. Taylor, and R. D. Averitt, "Active terahertz metamaterial devices," *Nature,* vol. 444, pp. 597-600, 2006.

[34] S. Zhang, W. Fan, K. J. Malloy, S. R. Brueck, N. C. Panoiu, and R. M. Osgood, "Near-infrared double negative metamaterials," *Opt. Express,* vol. 13, pp. 4922-4930, 2005.

[35] C. Caloz and T. Itob, *ELECTROMAGNETIC METAMATERIALS: Transmission line Theory and Microwave Applications*: Wiley-Interscience, 2006.

[36] M. Kafesaki, I. Tsiapa, N. Katsarakis, T. Koschny, C. M. Soukoulis, and E. N. Economou, "Left-handed metamaterials: The fishnet structure and its variations," *Physical Review B (Condensed Matter and Materials Physics),* vol. 75, pp. 235114-9, 2007.

[37] N. H. Shen, G. Kenanakis, M. Kafesaki, N. Katsarakis, E. N. Economou, and C. M. Soukoulis, "Parametric investigation and analysis of fishnet metamaterials in the microwave regime," *J. Opt. Soc. Am. B,* vol. 26, pp. B61-B67, 2009.

[38] X. Chen, T. M. Grzegorczyk, B.-I. Wu, J. Pacheco, and J. A. Kong, "Robust method to retrieve the constitutive effective parameters of metamaterials," *Physical Review E,* vol. 70, p. 016608, 2004.

[39] A. Minovich, D. N. Neshev, D. A. Powell, I. V. Shadrivov, and Y. S. Kivshar, "Tunable fishnet metamaterials infiltrated by liquid crystals," *Applied Physics Letters,* vol. 96, pp. 193103-193103-3, 2010.

[40] N. Vieweg, C. Jansen, M. K. Shakfa, M. Scheller, N. Krumbholz, R. Wilk, M. Mikulics, and M. Koch, "Molecular properties of liquid crystals in the terahertz frequency range," *Opt. Express,* vol. 18, pp. 6097-6107, 2010.

[41] P. G. Etchegoin, E. C. Le Ru, and M. Meyer, "An analytic model for the optical properties of gold," *The Journal of Chemical Physics,* vol. 125, pp. 164705-3, 2006.

[42] M. Ree, K. Chen, x, J, D. P. Kirby, N. Katzenellenbogen, and D. Grischkowsky, "Anisotropic properties of high-temperature polyimide thin films: Dielectric and thermal-expansion behaviors," *Journal of Applied Physics,* vol. 72, pp. 2014-2021, 1992.

[43] D. R. Smith, S. Schultz, P. Markoš, and C. M. Soukoulis, "Determination of effective permittivity and permeability of metamaterials from reflection and transmission coefficients," *Physical Review B,* vol. 65, p. 195104, 2002.

[44] D. R. Smith, D. C. Vier, T. Koschny, and C. M. Soukoulis, "Electromagnetic parameter retrieval from inhomogeneous metamaterials," *Physical Review E,* vol. 71, p. 036617, 2005.

[45] S. O'Brien and J. B. Pendry, "Magnetic activity at infrared frequencies in structured metallic photonic crystals," *Journal of Physics: Condensed Matter,* vol. 14, pp. 6383-6394, 2002.

[46] N. Liu, L. Fu, S. Kaiser, H. Schweizer, and H. Giessen, "Plasmonic Building Blocks for Magnetic Molecules in Three-Dimensional Optical Metamaterials," *Advanced Materials,* vol. 20, pp. 3859-3865, 2008.

[47] E. A. Yankovskaya, P. A. Belov, and C. R. Simovski, "Extraction of material parameters of multilayered nano-fishnet metamaterials from reflection and transmission coefficients," presented at the Metamaterials, 2008.

[48] T. Koschny, P. Markoscaron, D. R. Smith, and C. M. Soukoulis, "Resonant and antiresonant frequency dependence of the effective parameters of metamaterials," *Physical Review E,* vol. 68, p. 065602, 2003.

[49] L. Solymar and E. Shamon, *Waves in metamaterials*. Great British: OXFORD, 2009.

[50] P. U. Jepsen, D. G. Cooke, and M. Koch, "Terahertz spectroscopy and imaging – Modern techniques and applications," *Laser & Photonics Reviews,* vol. 5, pp. 124-166, 2011.

[51] R. YAHIAOUI, "Caractérisation de Métamatériaux pour Applications Millimétriques et Submillimétriques," DOCTEUR, Lasers, Matières et Nanosciences, L'UNIVERSITÉ DE BORDEAUX I, 2011.

[52] K. Sakai, *Terahertz Optoelectronics*. Tokyo: National Institute of Information and Communications Technology, 2005.

[53] T. D. Dorney, R. G. Baraniuk, and D. M. Mittleman, "Material parameter estimation with terahertz time-domain spectroscopy," *J. Opt. Soc. Am. A,* vol. 18, pp. 1562-1571, 2001.

[54] H. Němec, F. Kadlec, P. Kužel, L. Duvillaret, and J. L. Coutaz, "Independent determination of the complex refractive index and wave impedance by time-domain terahertz spectroscopy," *Optics Communications,* vol. 260, pp. 175-183, 2006.

[55] M. Naftaly and R. E. Miles, "Terahertz time-domain spectroscopy of silicate glasses and the relationship to material properties," *Journal of Applied Physics,* vol. 102, pp. 043517-6, 2007.

[56] M. Naftaly and R. E. Miles, "Terahertz Time-Domain Spectroscopy for Material Characterization," *Proceedings of the IEEE,* vol. 95, pp. 1658-1665, 2007.

[57] T. Kamei, N. Q. Dinh, and Y. Utsumi, "Microwave Polymer Dispersed Liquid Crystal Loaded Variable Phase Shifter," *Molecular Crystals & Liquid Crystals,* vol. 476, pp. 15-30, 2007.

Vita

Cheng-Ling (Brad) Chang was born in Kaohsiung, Taiwan R.O.C. He lived in many places including Taipei, Chia-Yi, Kaohsiung in Taiwan, and Seattle, Phoenix in U.S.A., and Hong Kong SAR. He earned his bachelor (2002) and master degree (2004) in Mechanical Engineering at National Chung-Cheng University, Taiwan. In 2012, he earned Doctor of Philosophy degree at University of Washington, Seattle in Mechanical Engineering.